

THESIS FOR THE DEGREE OF DOCTOR OF PHILOSOPHY

Phase-field modeling of stress-induced precipitation and
kinetics in engineering metals

CLAUDIO F. NIGRO



Department of Industrial and Materials Science
CHALMERS UNIVERSITY OF TECHNOLOGY
Gothenburg, Sweden 2020

Phase-field modeling of stress-induced precipitation and kinetics in engineering materials
CLAUDIO F. NIGRO
Gothenburg, Sweden, 2020
ISBN: 978-91-7905-337-6

© CLAUDIO F. NIGRO, 2020.

Doctoral thesis at Chalmers University of Technology
Series number 4804
ISSN 0346-718X

Department of Industrial and Materials Science
Chalmers University of Technology
SE-412 96 Gothenburg
Sweden
Telephone + 46 (0)31-772 1000

Printed by
Chalmers Reproservice
Gothenburg, Sweden 2020

Abstract

The formation of brittle compounds in metals operating in corrosive environments can be a tremendous source of embrittlement for industrial structures and such phenomenon is commonly enhanced in presence of stresses. To study this type of microstructural change modeling is preferred to experiment to reduce costs and prevent undesirable environmental impacts. This thesis aims at developing an engineering approach to model stress-induced precipitation, especially near stress concentrators, e.g. crack tips, for multi-phase and polycrystalline metals, with numerical efficiency.

In this thesis, four phase-field models are developed and applied on stress-induced hydride precipitation in zirconium and titanium alloys. The energy of the system is minimized through the time-dependent Ginzburg-Landau equation, which provides insights to the kinetics of the phenomenon. In these models, the driving force for precipitation is the coupling between the applied stress and the phase transformation-induced dilatation of the system. Models 1-3 implicitly incorporate near crack-tip stress fields by using linear elastic fracture mechanics so that only the phase-field equation is solved numerically with the finite volume method, reducing the computational costs. Phase transformation is investigated for intragranular, intergranular and interphase cracks in single- and two-phase materials by considering isotropy and some degrees of anisotropy, grain/phase boundary energy, different transition orders and solid solubility limit. Model 4 allows representing anisotropy connected to lattice mismatch and the orientation of the precipitates influenced by the applied stress. The model is employed through the finite element program Abaqus, where the fully coupled thermo-mechanical solving method is applied to the coupled mechanical/phase-field problem. Hydride growth is observed to follow the near-crack tip hydrostatic stress contours and can reach a steady state for specific conditions. The relation between hydride formation kinetics and material properties, and stress relaxation are well-reflected in the results.

With the presented approaches, precipitation kinetics including different kinds of defects, multi-phase microstructures, phase/grain boundaries, order transitions and loading modes can be successfully captured with low computational costs. They could therefore contribute to the numerical efficiency of multi-scale environment-assisted embrittlement prediction schemes within commercial software serving engineering projects.

Keywords: phase transformation, phase-field theory, corrosion, hydrogen embrittlement, hydride, linear elastic fracture mechanics, finite volume method, finite element method

A ma femme Pernilla et nos fils, Henri et Arthur,

To know that we know what we know, and to know that we do not know what we do not know, that is true knowledge.

- N. Copernicus



Faculty of Technology and Society

Department of Materials Science and Applied Mathematics

MALMÖ UNIVERSITY

Acknowledgements

This PhD work has taken place in the department of Material Science and Applied Mathematics at the Faculty of Technology and Society, Malmö University in cooperation with the department of Industrial and Materials Science at Chalmers University of Technology. This work was funded by Malmö University.

I would like to thank my supervisors, Christina Bjerkén, Ylva Mellbin and Pär Olsson, for supporting me throughout this project by providing their expertise, knowledge and encouragements. I am also grateful to the whole team within material science and mechanics at Malmö University for welcoming and integrating me with kindness and professionalism. I wish to give a special acknowledgement to my former colleague and friend Niklas Ehrlin who shared numerous exciting PhD student activities and interesting discussions.

I wish to thank my collaborators in the project CHICAGO (Crack-induced HydrIden nuCleation And GrOwth), which is a collaboration between the teams of Lund University and Malmö Univeristy. The members, Wureguli Rehemani, Martin Fisk, Christina Bjerkén, Per Ståhle, Pär Olsson and I, have allowed carrying out a common project and contributed to the writing of the appended Paper E.

Special and obvious thanks are addressed to my wife Pernilla and my two sons, Henri and Arthur, the brightest sunshines of my life, for their support and understanding. I am also grateful for the endless encouragements and additional support given by my parents, sister, brother, parents-in-law, cousins and closest friends.

Claudio Nigro
Malmö, Sweden

October 2020

List of publications

This thesis is based on the work contained in the following papers:

Paper A

Claudio F. Nigro, Christina Bjerken, Pär A. T. Olsson. Phase structural ordering kinetics of second-phase formation in the vicinity of a crack, **209**, 91–107. Published in the *International Journal of Fracture*, 2018.

Paper B

Claudio F. Nigro, Christina Bjerken, Pär A. T. Olsson. Kinetics of crack-induced hydride formation in hexagonal close-packed materials. Published in the *Proceedings of the 2016 International Hydrogen Conference*, 2016.

Paper C

Claudio F. Nigro, Christina Bjerken, Ylva Mellbin. Modelling of a Crack-Induced Hydride Formation at a Grain Boundary in Metals. Accepted for publication in the *International Journal of Offshore and Polar Engineering*, 2020.

This paper is an extension of:

Claudio F. Nigro, Christina Bjerken, Ylva Mellbin, Modelling of a Crack-Induced Hydride Formation near a Grain Boundary in Metals, Published in the *Proceedings of the 29th International Ocean and Polar Engineering Conference*, 2019

Paper D

Claudio F. Nigro, Christina Bjerken, Ylva Mellbin. Phase-field modelling: effect of an interface crack on precipitation kinetics in a multi-phase microstructure. Submitted to the *International Journal of Fracture*, 2020

Paper E

Wureguli Rehemani, Claudio F. Nigro, Martin Fisk and Christina Bjerken. Kinetics of Strain-Induced Precipitation - Phase-Field Model and Fully Coupled FE Approach. Manuscript form.

Own contribution

In Paper A, B, C and D, the author of this thesis carried out all simulations, numerical implementations and analyzed the results. He planned the entire work for Paper B, C and D. The co-authors participated in writing the manuscripts and planning the work for Paper A and contributed to the elaboration of all papers through discussions. For Paper E, the author of this thesis took an active part in the planning of the work, and worked on the numerical implementation, the development of the model and the manuscript writing.

Contents

1	Introduction	1
2	Environment-assisted degradation	3
2.1	Introduction to corrosion in metals	3
2.2	Hydrogen embrittlement	3
2.2.1	Forms of hydrogen damage	3
2.2.2	Hydride formation in titanium- and zirconium-based metals	4
2.2.3	Stress-induced hydride formation and delayed hydride cracking	6
2.2.4	Effect of phase/grain boundaries on hydride formation	6
2.2.5	Hydridation of a bi-phase metal: the Ti-6Al-4V	6
3	Linear elastic fracture mechanics	8
3.1	Crack in homogeneous materials	8
3.2	Interface cracks	11
4	Introduction to phase-field theory	13
4.1	The phase-field variables	14
4.2	Minimization of the free energy of a system	15
4.2.1	The total free energy	15
4.2.2	The bulk free energy density	15
4.2.3	First- and second-order transitions	18
4.2.4	Multi-phase and multi-order-phase systems	19
4.2.5	The kinetic equations	19
5	Phase-field models to predict stress-induced precipitation kinetics	21
5.1	Model 1: Sixth order Landau potential for crack-induced second-phase formation modeling	22
5.2	Models 2 and 3: Stress-induced precipitation at grain/phase boundaries	25
5.3	Model 4: Stress-induced second-phase formation modelling applied to commercial software	29

5.4	Summary and comparison of the main features of the models when applied to crack-induced precipitation	30
5.5	Numerical solution strategies and boundary conditions	31
5.5.1	Model 1, 2 and 3	31
5.5.2	Model 4	32
6	Summary of the appended papers	33
6.1	Paper A	33
6.1.1	The analytical steady-state solution	33
6.1.2	Numerical results	34
6.1.3	Further remarks	35
6.2	Paper B	36
6.3	Paper C	37
6.4	Paper D	39
6.4.1	Analysis of the model	39
6.4.2	Numerical results	41
6.5	Paper E	43
6.5.1	Second-phase formation in a defect-free medium	43
6.5.2	Further works and remarks	45
7	Discussion and future works	46
7.1	Assets	46
7.2	Discussions	47
7.3	Future works	48
8	Conclusion	50
	Bibliography	51

1 Introduction

Hydrogen, the most abundant and lightest chemical element in the universe, has become a major concern for the material industry. Numerous works have shown that it is responsible for degrading the mechanical properties of metals in hydrogen-rich environments, possibly leading to premature fracture [1].

Hydrogen embrittlement (HE) is generally characterized by the deterioration of the mechanical properties of a material in presence of hydrogen. The phenomenon is well-known in aerospace and nuclear industries. In rocket engines, developed for Ariane 6 such as Vinci and Vulcain 2, hydrogen is thought to be utilized as fuel and cooler and, therefore, interacts with some engine components. The mechanical properties of nickel-based superalloys, traditionally used in high-temperature areas such as the combustion chamber [2] and the nozzle, have been observed to be derogated in presence of hydrogen [3, 4]. Brittle compounds, titanium hydrides, are likely to form in colder engine parts made of titanium alloys when in contact with hydrogen and can embrittle the structure. In nuclear reactor pressure vessels, atomic hydrogen (H) penetrates zirconium-based cladding and pressure tubes, where brittle zirconium hydrides potentially form [5, 6]. Hydride formation is one stage of the complex mechanism of delayed hydride cracking (DHC) [7, 8], which is one of the most notorious mechanisms of HE in nuclear industry. Hydride precipitation, strongly influenced by the presence of stress [9], can be enhanced by the presence of material defects acting as stress concentrators [10]. Knowledge of hydride formation kinetics is fundamental in order to predict the lifetime of a metallic structure subjected to hydride-based failure processes, such as DHC in a hydrogen-rich environment. Modeling is found to be an economically beneficial route to study the growth of hydride phase regions in a metallic structure operating in a hydrogen-rich environment and under applied load. Second-phase formation has been modeled over the years through the use of different approaches such as the sharp-interface and phase-field methods (PFM). The latter is found to be more practical to model complex microstructures with numerical efficiency and can include stress effect on precipitation [11, 12, 13].

This thesis is included in a project, which aims at building an engineering tool to model stress-induced precipitation and kinetics, and to design the product to be numerical efficient and easily implementable in commercial software. Within this framework, the objective of the work is to develop a numerical approach for modeling of precipitation, especially in the vicinity of stress concentrators, such as crack tips, and at grain and phase boundaries.

In the present thesis, different approaches based on phase-field theory (PFT) are developed. Linear elastic fracture mechanics (LEFM) is adopted in three of the four presented models in order to account for the stress field near an opening sharp crack. With these models, many aspects such as the solid solubility limit, the transition temperature, the interfacial energy, the applied stress, the energy of phase and grain boundaries, the transition order and some forms of anisotropy are incorporated in the considered problems, which are solved by using the finite volume method (FVM). These approaches are also flexible in terms of applications and formulated optimally such that the considered microstructural evolutions are captured with

numerical efficiency. The latter is partly due to the fact that only the equation related to phase transformation needs to be solved numerically while mechanical equilibrium is calculated analytically. The fourth approach is still a pilot model and is written to account for stress-induced second-phase formation, where the anisotropic dilatation of the material caused by phase transformation in relation with the orientation of the second-phase regions is addressed. With this model, the applied stress and defects are represented explicitly by choosing appropriate meshes and boundary conditions. The coupled mechanical and phase field-related equations are solved simultaneously by using the finite element method (FEM) associated to a fully coupled approach similar to that employed to solve thermo-mechanical problems. The application of the numerical methodology to the presented problems has been made possible thanks to the capacities and customizable subroutines of the commercial software Abaqus [14].

In this work, all mathematical approaches are applied to model stress-induced hydride formation. Crack-induced hydride formation is regarded with models 1-3 while hydride precipitation in a hydrogenated defect-free medium and near a notch tip is considered with model 4. Nevertheless, all presented models could also be employed to study environment-assisted degradation mechanisms, other than HE, involving the precipitation of brittle phases in materials operating in corrosive environment, e.g. rust or carbide formation in steel.

In this PhD thesis, the physical aspects and mathematical tools as the basis of this work are presented before the different models introduced above are described. Thereafter, the results obtained in the papers are reported and thoughts about futures developments are discussed. Parts of this document are taken and/or rephrased from the author's licentiate thesis [15].

2 Environment-assisted degradation

2.1 Introduction to corrosion in metals

In operation, most metallic structures are observed to interact with their environments. Such interactions can affect the appearance of the metals and their physical properties, e.g. their mechanical properties. Corrosion is one deteriorative process, which is characterized by a destructive, unintentional and electrochemical attack of metals usually starting at their surface. There are several forms of corrosion such as uniform attack, galvanic corrosion, crevice corrosion, pitting, erosion-corrosion, selective leaching, intergranular corrosion, stress corrosion and HE [16].

Through intergranular corrosion, some stainless-steel structures experience failure along their grain boundaries. In the latter region, chromium, usually added to increase corrosion resistance, reacts with carbon to form chromium carbide. The regions adjacent to the grain boundary result depleted of chromium and, consequently, become more vulnerable to corrosion. The grain and phase boundaries are usually preferential site for precipitation because the nucleation energy barrier is lower and diffusion is quicker therein [17].

Some materials, which usually do not experience any form of corrosion in corrosive environments, can display reaction of corrosion when subjected to tensile stress or residual stresses. Cracks can nucleate in these areas, propagate and possibly lead to structure failure. This form of corrosion is named stress corrosion and the phenomenon is commonly referred to as stress corrosion cracking. In steels, rust, a brittle phase with lower fracture toughness than the rest of the material, can appear in material regions where stress is located and, subsequently, fracture. For instance, iron oxide can be seen to precipitate in welds and pipe bends, where residual stresses reside. Stress corrosion cracking results in brittle fracture regardless of the degree of ductility of the affected metal and may occur for stresses significantly below the fracture toughness [16].

2.2 Hydrogen embrittlement

2.2.1 Forms of hydrogen damage

The presence hydrogen in metals, such as steels, aluminum (Al), titanium (Ti), zirconium (Zr), nickel (Ni) and their respective alloys, can alter the properties of the material. As for stress corrosion, failures can arise from residual and/or applied tensile stresses combined with hydrogen-metal interactions in hydrogen-rich environments. Such interactions are commonly found to cause loss of ductility and reduction of load-carrying capacity in a metal. The term hydrogen embrittlement is used to refer to such deteriorations of materials. Stress corrosion and HE are similar in that normally ductile materials undergo brittle fracture when subjected to stress and corrosive environment. One difference between the two phenomena is that stress corrosion usually occurs in material regions, where anodic reactions take place, while hydrogen environment embrittlement can be initiated or enhanced by cathodic reactions, e.g. in the presence of a cathodic protection. Hydrogen environment embrittlement characterizes situations where materials undergo plastic deformation, while in contact with hydrogen-rich

gases or corrosion reactions. Molecular hydrogen experiences adsorption at the metal free surface, which weakens the H-H bond and favors its dissociation into atomic hydrogen within the metal lattice [18, 19]. Several other types of hydrogen damage mechanisms are known as hydrogen attack, blistering, and hydride formation [1], hydrogen enhanced localized plasticity (HELP) and hydrogen-induced decohesion (HID). Hydrogen attack usually affects steels at high temperature. The inner hydrogen reacts with carbon to form methane within the material. Possible damaging consequences are crack formation and decarburization. Blistering is the result of plastic deformation induced by the pressure of molecular hydrogen that is formed near internal defects. The gas formation occurs due to the diffusion of atomic hydrogen to these regions. Once formed, blisters are often observed to be fractured. The HELP mechanism is characterized by an enhancement of the mobility of dislocations by interaction with hydrogen [20]. In other cases, the presence of hydrogen can induce a reduction in the bonding energy between atoms, which consequently increases the risk of decohesion [21]. This mechanism is the so-called HID.

2.2.2 Hydride formation in titanium- and zirconium-based metals

During service and in presence of hydrogen, the formation of brittle and non-metallic compounds, the so-called hydrides, can be responsible for material embrittlement [5, 7, 22]. A number of materials such as zirconium, titanium, hafnium, vanadium and niobium are considered as hydride forming metals as they have a low solubility of hydrogen, and, therefore, can form different types of hydride phases depending on e.g. hydrogen concentration and temperature history [8]. This section is focused on briefly describing hydridation and its effect on mechanical properties in Zr- and Ti-based metals.

Pure titanium and zirconium microstructures have two different possible crystal structures: α , a hexagonal close-packed (HCP) microstructure at low temperature, and β , a body-centered cubic (BCC) microstructure at elevated temperatures. For pure Ti and Zr, the transition between these phases occurs through an allotropic transformation at 882°C and 862°C respectively. The dissolution of alloying elements can be done to stabilize different phases by modifying the α - β transition temperature or to cause solid solution strengthening. While a number of interstitial elements such as nitrogen, carbon, and oxygen act as α -stabilizers, the addition of hydrogen to the solid solution induces the stabilization of the β -phase by lowering the transus temperature. This can also be seen when considering the Zr-H and the Ti-H phase diagrams in Figure 1. The solid solution phase α has a low solubility of hydrogen while the high-temperature allotrope β -Zr has a high solid solubility limit. In fact, for Ti, phase α possesses a maximum solubility of hydrogen equal to 4.7 at.% and for phase β it is equal to 42.5 at.% at 298°C. This can be imputed to the affinity of hydrogen for tetrahedral interstitials, which are twelve in the BCC phase and four in the HCP one [23]. For a given concentration of hydrogen and range of temperature, the phase diagrams exhibit regions of existence and stability (or metastability) of hydride phases [24, 25]. For both metals, two stable hydride phases are identified to be the face-centered cubic (FCC) δ -phase and the face-centered tetragonal (FCT) ϵ -phase. The γ -phase is considered metastable and has an FCT structure [26, 27]. Additionally, for the Zr-H system, a crystal structure denoted ζ has been observed and may be a possible precursor to the formation of γ - and δ -phases [28]. The Ti-

hydride χ , which forms at 41-47 at.% hydrogen at temperatures around -200 °C is rarely observed [23].

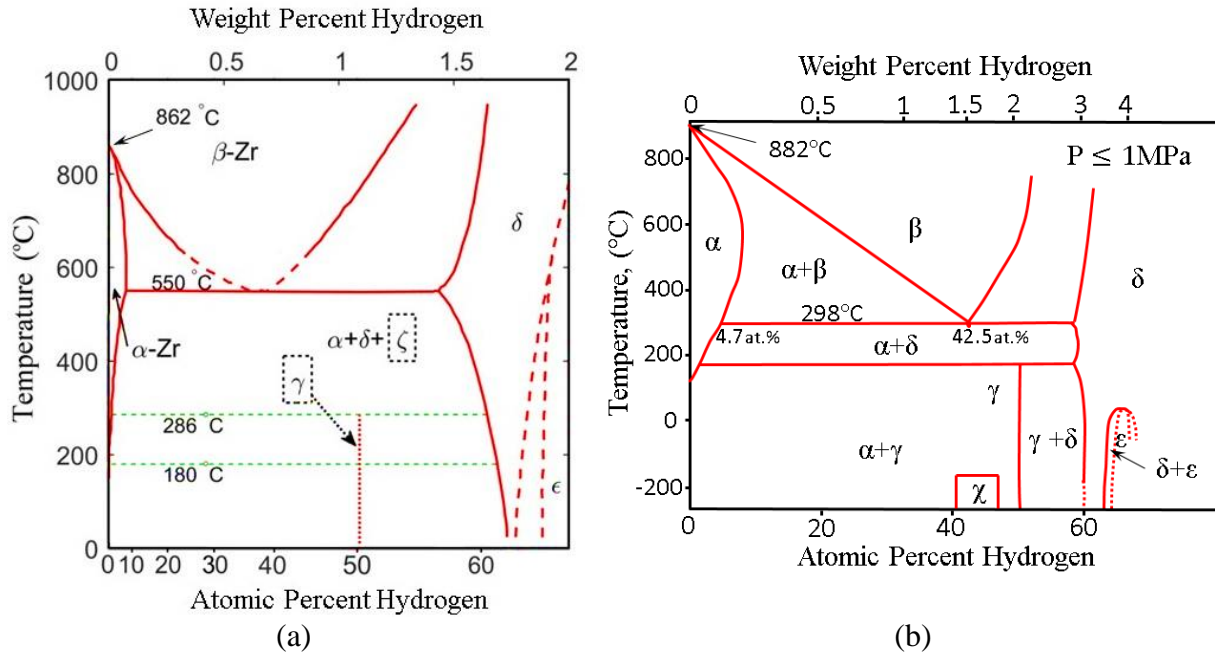


Figure 1: Phase diagram for (a) the Zr-H system, (reproduced and modified with permission from [29]), and (b) the Ti-H system (sketch based on [25]).

The hydride precipitates generally appear as needles or platelets in the α -phase, and the formation can occur either in grains or grain/phase boundaries in polycrystals [5, 8, 30, 31]. A preferred hydride orientation may exist and is affected by the crystal structure and texture emanating from the manufacturing process and the possible presence of applied and residual stresses [7, 9]. Under a sufficiently high applied load, the hydride platelets usually form perpendicular to the applied stress [6].

Some hydrides such as δ - and γ -hydrides in Zr- and Ti-based alloys exhibit a volume change when they form [26, 27]. For instance, the global swelling of the unconstrained δ - and γ -Zr hydrides, which results from anisotropic dilatational misfits, has been theoretically estimated to be between 10% and 20% with respect to untransformed zirconium [32]. The deformations induced by phase transformation can also be referred to as eigenstrains, stress-free strains or phase-transformation strains. The hydrides are more brittle than the α -phase, and the fracture toughness of a hydride can be orders of magnitude lower than the solid solution. For example, the fracture toughness K_{IC} of pure α -Ti at room temperature is around $60 \text{ MPa} \cdot \text{m}^{1/2}$ [33] while for titanium-based δ -hydride the value of K_{IC} can be found between 0.72 and $2.2 \text{ MPa} \cdot \text{m}^{1/2}$ [34, 35]. The Zr-2.5Nb alloy's fracture toughness was measured to be around $70 \text{ MPa} \cdot \text{m}^{1/2}$ with quasi-zero hydrogen content, while that of the δ -hydride (ZrH_x , $x = 1.5\text{--}1.64$) is found to be approximately $1 \text{ MPa} \cdot \text{m}^{1/2}$ at room temperature [36, 37]. In addition, as the hydrogen content increases, the overall fracture toughness of hydrided metals may decrease. For instance, the fracture toughness of the Zr-2.5Nb alloy with a hydrogen-zirconium atomic ratio of 0.4, is mostly found between 5 and $15 \text{ MPa} \cdot \text{m}^{1/2}$ [36].

2.2.3 Stress-induced hydride formation and delayed hydride cracking

In structures operating under applied stress, hydridation has been observed to be facilitated. Of great concern is that these brittle compounds are often observed to form in high stress concentration regions, such as in the vicinity of notches, cracks and dislocations, where the material solubility limit is exceeded [38, 39, 40, 41, 42, 43]. Under stress and deformation of the metal, and owing to their low fracture toughness, hydride platelets can be fractured along their length, e.g. in Ti [42, 44], in Zr: [41, 45], in Hf [46]; in V: [38, 47]; and in Nb: [48], or across their thickness, e.g. in Ti: [49] and in Zr: [22, 50]. A well-known associated fracture mechanism example is the so-called delayed hydride cracking (DHC). It is a form of localized hydride embrittlement under applied stress that is characterized by a combination of processes, which involve hydrogen diffusion, hydride precipitation including subsequent material expansion – the phase transformation induces a swelling of the reacting zone – and crack growth [8]. Driven by the stress gradients, hydrogen migrates in the vicinity of defects, e.g. residual stresses or crack tips, leading to supersaturation. Brittle hydrides form once the solid solubility limit is exceeded and usually develop orthogonally to the tensile stress until a critical size is reached. Then, cleavage takes place in the localized hydrided region and the crack propagation stops at the hydride/solid solution interface. Crack propagation progresses stepwisely by repeating this process [5]. The adjective “delayed” reflects the fact that it takes time for hydrogen to diffuse towards the crack tip and react with the matrix to form a hydride [27]. For instance, DHC was observed to operate in Zr-2.5Nb alloy pressure tubes in nuclear industry [51].

2.2.4 Effect of phase/grain boundaries on hydride formation

As seen earlier while describing intergranular corrosion, phase and grain boundaries are preferential precipitation regions. In the context of HE, hydrogen diffuses more easily and the nucleation energy barrier is lower therein than within the crystals. Precipitation at phase/grain boundaries has been observed for instance in zirconium and titanium alloys [5, 31, 52, 53, 54, 55].

2.2.5 Hydridation of a bi-phase metal: the Ti-6Al-4V

Titanium alloys are frequently use in aerospace industry because of their good thermo-mechanical properties and their low weight. For one of them, the Ti-6Al-4V, also named Ti64, both the α - and β -phases are found stable at room temperature. For this particular alloy, aluminum (Al) is an α -stabilizer and vanadium (V) is a β -stabilizer. The microstructure of Ti64 can vary significantly depending on the thermo-mechanical treatment. More extensive information about the relationship between the microstructure of Ti64 and its thermo-mechanical treatment can be found, for instance, in [23, 56]. A typical microstructure of Ti64 is presented in Figure 2. This microstructure contains globular α and lamellar ($\alpha+\beta$) regions. In this example, the ($\alpha+\beta$) regions are also referred to as α colonies. In this thesis, the interfaces between the different phases in Ti64 are termed in the following manner: grain boundaries denote the interface that separate two α -grains whereas phase boundaries separate α -phase regions from β -phase ones.

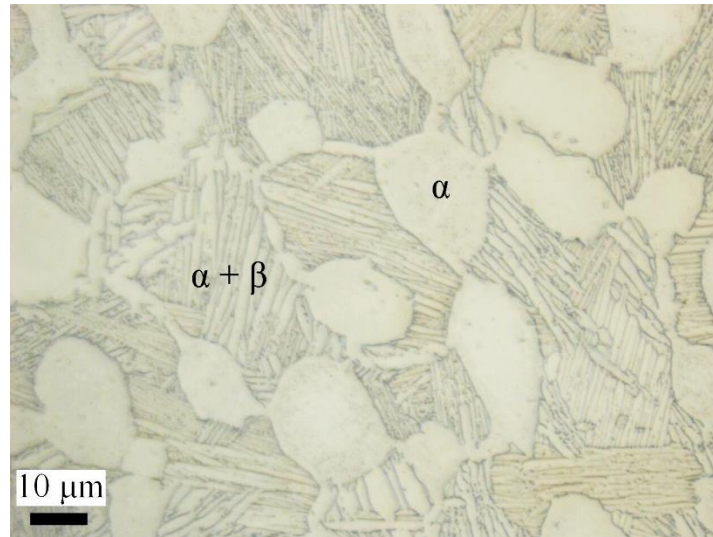


Figure 2: Optical micrograph of a Ti-6Al-4V microstructure from a sample prepared as described in [57].

The solubility of hydrogen and the diffusion rate in $(\alpha+\beta)$ -Ti alloys are different from one phase to another. Phase α has a much lower solubility of hydrogen than phase β and hydrogen diffuses faster in the phase β than in phase α . For example, at room temperature the hydrogen diffusion rate is $1.45 \cdot 10^{-16} \text{ m}^2/\text{s}$ in the α -phase and $5.45 \cdot 10^{-12} \text{ m}^2/\text{s}$ in the β -phase. Because of the differences in diffusion rate and terminal solubility between phase α and β , a high diffusion rate in the phase interfaces, and the fact that the phase/grain boundaries are preferential nucleation sites, hydride formation is facilitated at α/β and α/α interfaces compared to the rest of the material [27, 31, 54]. Hence, these locations, naturally more susceptible to fracture than the rest of the material under stress, result even more weakened in presence of hydrogen. For these reasons, hydrogen-induced cracking is expected to mostly occur in phase α and along the grain/phase boundaries. In fact, this observed in Ti64 in [58]. Some recent observations also indicate the possible presence of hydrides other than δ or γ at the phase boundaries [54].

3 Linear elastic fracture mechanics

In operation, mechanical components and structures can undergo damages, which commonly take the form of micro-cavities and cracks. Failure mechanisms involved in fracture have been studied extensively and a number of models have been formulated throughout the 20th century [59, 60, 61, 62, 63, 64]. In 1957, a theory, the so-called linear elastic fracture mechanics (LEFM), providing a two-dimensional description of the stresses and displacements ahead of a crack was developed [65]. The high stresses residing at and around a crack-tip can generate plastic deformations and other nonlinear effects in many metals. Linear elastic fracture mechanics is formulated for “small scale yielding”, i.e. for cases for which the size of the nonlinearity zone around the crack-tip does not exceed a fraction of a characteristic dimension such as the crack length.

3.1 Crack in homogeneous materials

In a homogeneous material, the analytical expressions for the stress and displacement field components provided by LEFM include a multiplying factor, known as the stress intensity factor, which depends on the external stress, the crack length and the geometry of the considered structure, and is related to the energy release rate. The stress intensity factor can be different depending on the considered mode of fracture. There are three basic modes of fracture, which are depicted in Figure 3. Mode I designates the tensile opening mode, which is characterized by the symmetric separation of the crack walls with respect to the plane formed by the crack axis and crack front. Mode II, also called the in-plane sliding mode, is described by a shear stress parallel to the crack plane and perpendicular to the crack front. In mode III, also known as the tearing or anti-plane shear mode, the shear stress acts in the crack plane and parallel to the crack front. In real problems, cracks are usually found to open in mixed modes.

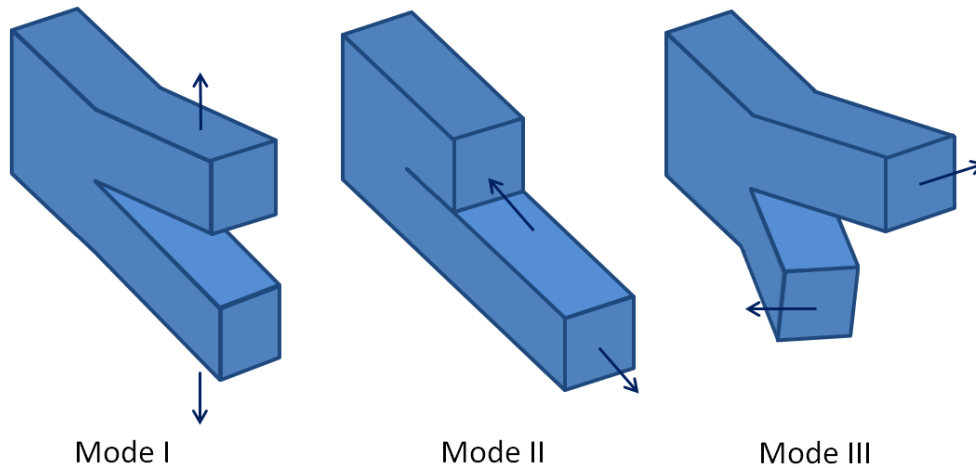


Figure 3: Illustration of the three fracture modes.

The expression of the stress field components in the vicinity of the crack-tip lying in a homogeneous linear elastic medium for a specific mode of fracture can be written as in [66] as

$$\sigma_{ij} = \frac{K}{\sqrt{2\pi r}} f_{ij}(\theta) + \sum_{m=0}^{\infty} B_m r^{\frac{m}{2}} g_{ij}^{(m)}(\theta), \quad (1)$$

where K is the stress intensity factor for the considered mode, f_{ij} is an angular function, B_m and the dimensionless function $g_{ij}^{(m)}$ respectively designate the stress-dependent coefficient and a trigonometric function for the m^{th} term. The quantities r and θ are the polar coordinates, for which the origin is placed at the crack tip as illustrated in Figure 4. The indices i and j are taken in $\{x, y\}$ to obtain the expression of the stress field components in a Cartesian base, whereas if a polar base is considered, then $i, j \in \{r, \theta\}$. A representation of the stresses in these two different bases is given in Figure 4. At a sufficiently small distance from the crack tip, the high-order terms of the right hand side of Eq. (1) are negligible with respect to the first one. In this condition, the stress can be assumed to vary as $1/\sqrt{r}$. In case of an infinite plane containing a $2a_0$ long crack opening in mode I, $K = \sigma_{yy}^{\infty} \sqrt{\pi a_0}$, where σ_{yy}^{∞} is a tensile stress applied remotely and perpendicular to the crack surfaces.

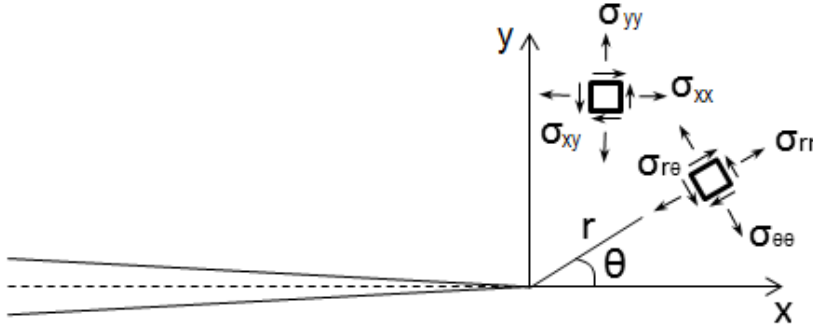


Figure 4: Illustration of the two-dimensional stress in different coordinate systems and bases in the vicinity of a crack tip.

For a linear elastic medium, Hooke's law provides a linear relation between the strain tensor ε_{ij} and the stress tensor as

$$\varepsilon_{ij} = S_{ijkl} \sigma_{kl} \text{ or } \sigma_{ij} = c_{ijkl} \varepsilon_{kl} \quad (2)$$

where s_{ijkl} and c_{ijkl} are the compliance tensor and the stiffness tensor respectively. By considering small deformation, the strain tensor is connected to the displacement field u_i through the expression

$$\varepsilon_{ij} = \frac{1}{2} \left(\frac{\partial u_i}{\partial x_j} + \frac{\partial u_j}{\partial x_i} \right). \quad (3)$$

The out-of-plane stress and strain are affected by the considered plane-state condition. The plane stress state is suitable to represent mechanical problems occurring at the surface (or near surface) of thick bodies or in thin media as the stress components relative to the out-of-plane direction is zero. In contrast, the plane strain state is suited to represent mechanical problems taking place within the volume of a thick body as the strain components relative to the out-of-

plane direction are zero. In summary, in plane stress $\sigma_{zz} = 0$ and $\varepsilon_{zz} = -\nu(\sigma_{xx} + \sigma_{yy})/E$ and in plane strain, $\sigma_{zz} = \nu(\sigma_{xx} + \sigma_{yy})$ and $\varepsilon_{33} = 0$, where ν and E are the Poisson's ratio and the Young's modulus.

Considering fracture in mode I, the angular functions of Eq. (1) for an isotropic and linear elastic body in a Cartesian base are expressed as [66],

$$f_{xx}(\theta) = \cos \frac{\theta}{2} \left[1 - \sin \frac{\theta}{2} \sin \frac{3\theta}{2} \right], \quad (4)$$

$$f_{yy}(\theta) = \cos \frac{\theta}{2} \left[1 + \sin \frac{\theta}{2} \sin \frac{3\theta}{2} \right], \quad (5)$$

$$f_{xy}(\theta) = \sin \frac{\theta}{2} \cos \frac{\theta}{2} \cos \frac{3\theta}{2}. \quad (6)$$

The associated displacement field for such body is given as

$$u_x = \frac{K_I (1 + \nu)}{E} \sqrt{\frac{r}{2\pi}} \cos \frac{\theta}{2} \left[\kappa_0 - 1 + \sin^2 \frac{\theta}{2} \right], \quad (7)$$

$$u_y = \frac{K_I (1 + \nu)}{E} \sqrt{\frac{r}{2\pi}} \sin \frac{\theta}{2} \left[\kappa_0 + 1 - \cos^2 \frac{\theta}{2} \right], \quad (8)$$

where $\kappa = 3 - 4\nu$ in plane strain and $\kappa = (3 - \nu)/(1 - \nu)$.

A description of the anisotropic linear-elastic stress field in proximity of a crack tip has been developed by Paris and Sih [67]. According to their theory, for anisotropic and homogeneous bodies undergoing a fracture in mode I, σ_{ij} can be expressed through the use of Eq. (1) with

$$f_{xx}(\theta) = \text{Re} \left\{ \frac{\mu_1 \mu_2}{\mu_1 - \mu_2} \left(\frac{\mu_2}{\sqrt{\cos \theta + \mu_2 \sin \theta}} - \frac{\mu_1}{\sqrt{\cos \theta + \mu_1 \sin \theta}} \right) \right\}, \quad (9)$$

$$f_{yy}(\theta) = \text{Re} \left\{ \frac{1}{\mu_1 - \mu_2} \left(\frac{\mu_1}{\sqrt{\cos \theta + \mu_2 \sin \theta}} - \frac{\mu_2}{\sqrt{\cos \theta + \mu_1 \sin \theta}} \right) \right\}, \quad (10)$$

$$f_{xy}(\theta) = \text{Re} \left\{ \frac{\mu_1 \mu_2}{\mu_1 - \mu_2} \left(\frac{1}{\sqrt{\cos \theta + \mu_1 \sin \theta}} - \frac{1}{\sqrt{\cos \theta + \mu_2 \sin \theta}} \right) \right\}, \quad (11)$$

where Re is the real part of a complex number, and μ_1 and μ_2 are the conjugate pairs of roots of

$$S_{11} \mu^4 - 2S_{16} \mu^3 + (2S_{12} + S_{66}) \mu^2 - 2S_{26} \mu + S_{22} = 0. \quad (12)$$

When $\mu_1 = \mu_2$, the stress field relations boils down to the isotropic ones. The coefficients S_{ij} are the in-plane compliance components in a given crystal plane, such that

$$\begin{bmatrix} \varepsilon_{xx} \\ \varepsilon_{yy} \\ 2\varepsilon_{xy} \end{bmatrix} = \begin{bmatrix} S_{11} & S_{12} & S_{16} \\ S_{12} & S_{22} & S_{26} \\ S_{61} & S_{62} & S_{66} \end{bmatrix} \begin{bmatrix} \sigma_{xx} \\ \sigma_{yy} \\ \sigma_{xy} \end{bmatrix}, \quad (13)$$

and are combinations of the three-dimensional compliance components s_{ijkl} . The displacements in the vicinity of the crack tip can subsequently be deduced by using Eqs.(9)-(13).

3.2 Interface cracks

An interface between two solids of dissimilar material is commonly a low-toughness fracture path in various materials. A number of investigations about the crack-tip fields in bi-material interface crack problems, as that illustrated in Figure 5, have been carried out in the previous century [68, 69, 70, 71, 72, 73, 74, 75, 76]. An outcome of these studies is the formulation of analytical expression for a two-dimensional near crack-tip stress field as [76],

$$\sigma_{ij} = \frac{1}{\sqrt{2\pi r}} \left[\text{Re}(K^* r^{J\omega}) \Sigma_{ij}^I + \text{Im}(K^* r^{J\omega}) \Sigma_{ij}^{II} \right], \quad (14)$$

where $i, j \in \{x, y\}$, J is the complex number, i.e. $J = \sqrt{-1}$, and the tensors components Σ_{ij}^I and Σ_{ij}^{II} are the angular functions, whose expressions can be found in polar coordinates in [76] and in Cartesian coordinates in [77]. The oscillatory parameter ω is defined as

$$\omega = \frac{1}{2\pi} \ln \left[\frac{1 - \beta_0}{1 + \beta_0} \right], \quad (15)$$

where β_0 is a Dundurs parameter and is expressed as [78],

$$\beta_0 = \frac{\mu_1(\kappa_2 - 1) - \mu_2(\kappa_1 - 1)}{\mu_1(\kappa_2 + 1) + \mu_2(\kappa_1 + 1)}, \quad (16)$$

where μ_i ($i = 1, 2$) is the shear modulus in the material i , assumed elastic and isotropic, as depicted in Figure 5, and $\kappa_i = 3 - 4\nu_i$ in plane strain and $\kappa_i = (3 - \nu_i)/(1 - \nu_i)$ in plane stress. The parameter ν_i is the Poisson's ratio in the material i . The parameter K^* is named complex interface stress intensity factor as can be seen as a substitute to the mode-I and mode-II stress intensity factors in case of a crack lying in a homogeneous material [79].

At the right hand tip of an isolated crack of length $2a_0$ lying along the interface between two semi-infinite planes subjected to remote stresses σ_{yy}^∞ and σ_{xy}^∞ as displayed in Figure 5, the complex stress intensity factor can be written as [76],

$$K^* = (\sigma_{yy}^\infty + J\sigma_{xy}^\infty)(1 + 2J\omega)\sqrt{\pi a_0} (2a_0)^{-J\omega}. \quad (17)$$

The term $K^* r^{J\omega}$ in Eq. (14) oscillates with r for $r \rightarrow 0$. This results in possible zones of contact or interpenetration for sufficiently small r . This oscillatory problem has been studied over the years and a review on the topic is provided in [80]. Rice et al. (1990) gives an

estimation of the distance r_{con} over which interpenetration or zone of contact takes place [76]. For $\omega > 0$, r_{con} is expressed through the relation

$$r_{\text{con}} \cong 2 L e^{-\frac{\psi^* + \frac{\pi}{2}}{\omega}}, \quad (18)$$

where L is a reference length and ψ^* is the phase angle of $K^* r^{J\omega}$. For $\omega < 0$, the parameter ω must be change into $-\omega$ and ψ^* into $-\psi^*$.

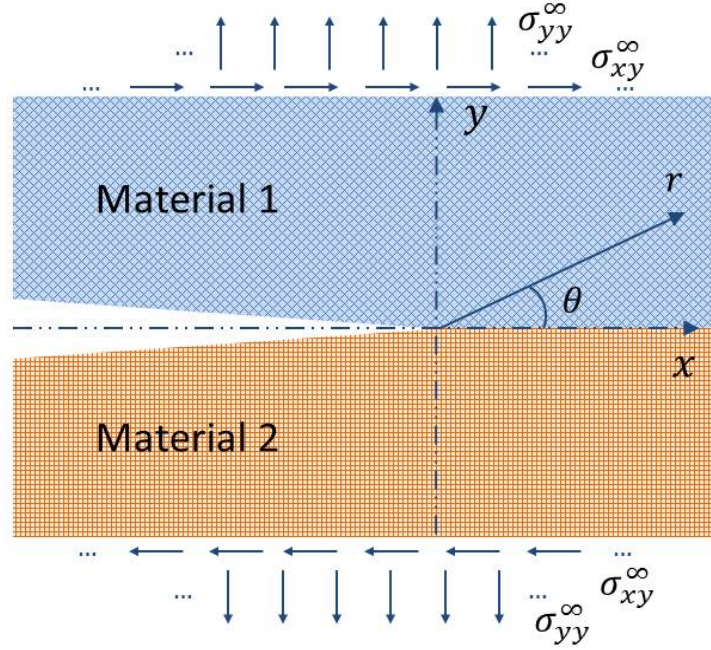


Figure 5: Geometry of an interface crack.

Rice et al. (1990) states that the formulation using complex interface stress intensity factor can be considered valid if the range of r considered in an analysis is small compared to a reference length, such as the crack length, and sufficiently large compared to the near crack-tip contact zone. For many combinations of materials, r_{con} can be subatomic, e.g. it can be smaller than an atomic spacing for a few millimeter-long crack.

4 Introduction to phase-field theory

Material processing, including solidification, solid-state precipitation and thermo-mechanical processes, is the origin of the development of material microstructures. The latter generally consists of assemblies of grains or domains, which vary in chemical composition, orientation and structure. Characteristics of the microstructure such as shape, size and distribution of grains, impurities, precipitates, pores and other defects have a strong impact on the physical properties (e.g. thermal and electrical conductivity) and the mechanical performance of materials. Therefore, the study of mechanisms causing microstructural changes appears necessary to predict the modifications of material properties and, thus, take action to avoid associated malfunctioning components or failure of structures.

Conventionally, the physical and thermodynamic mechanisms acting in an evolving microstructure such as heat diffusion and impurity transportation are modeled through the use of time-dependent partial differential equations and associated boundary conditions. This is, for instance, the case in sharp-interface approaches, where the interfaces between the different microstructure areas are represented by a discontinuity, as shown in Figure 6a, and their positions need to be explicitly followed with time. However, some phenomena are not suitable for sharp-interface modeling when they are combined with other effects [81]. In addition, complex morphologies of grains are hard to represent mathematically by the sharp-interface approaches when the interfaces interact with each other during phase transformation, e.g. interface merging and pinch-off within coalescence and splitting of precipitates. Moreover, such modeling is found to be more computationally demanding than diffuse-interface approaches. Therefore, sharp-interface models are often more appropriate for one-dimensional problems or simple microstructural topologies [11, 82].

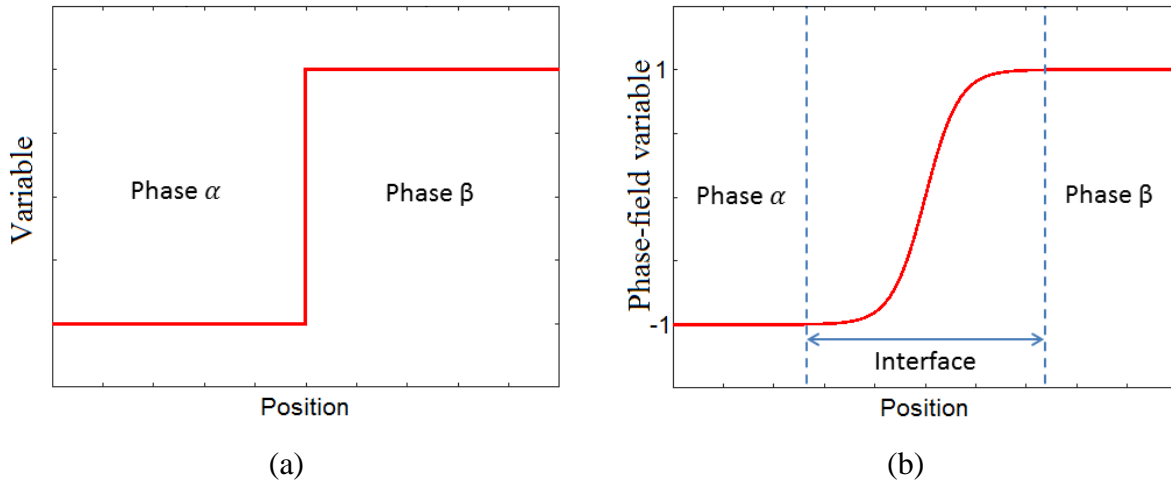


Figure 6: Illustration of (a) a sharp interface and (b) a smooth interface.

An alternate way to describe the microstructure evolution is to use phase-field methods (PFM), which also employ kinetics equation. This type of modeling provides a continuous and relatively smooth description of the interfaces, as illustrated in Figure 6b. The microstructure is represented by variables, also called phase-field variables, which are continuous through the interfaces and are functions of time and space. Thus, unlike sharp interface models, the position of the interface is implicit and determined by the variation of

the variable value. Moreover, no boundary conditions are necessary inside the whole system except at the system boundary. Initial conditions are, however, still required. Consequently, PFT allows not only the description of the evolution of simple but also complex microstructural topologies unlike sharp-interface problems. For instance, the dendritic solidification with its complex features was successfully modeled through the use of PFM [83, 84].

Lately, phase-field modeling has found numerous applications in magnetism and material science processes such as solidification, solid-state phase transformation, coarsening and grain growth, crack propagation, dislocation dynamics, electro-migration, solid-state sintering and processes related to thin films and fluids. A number of these achievements, and comprehensive descriptions and reviews of phase field modeling can be found in [11, 82, 85, 86, 87, 88, 89]. More recent publications show that PFM is a current research field when it comes to modeling phenomena which involve some of the mechanisms listed in this paragraph [90, 91, 92, 93, 94, 95, 96, 97, 98, 99].

4.1 The phase-field variables

In PFT, a microstructural system is described through the use of single or multiple phase-field variables. Depending on the type of quantity it is connected to, a phase-field variable can be conserved or non-conserved. Conserved variables customary refer to local composition quantities, e.g. the concentration or the mass of chemical species. They can also be associated with density and molar volume [87]. According to Moelans et al. (2008), the non-conserved phase-field variable category contains two groups of variables ϕ : the phase-fields and the order parameters [82]. Both groups are utilized to distinguish two concurrently prevailing phases. The phase-fields are phenomenological parameters indicating the presence of a phase at a specific position and the order parameters designate the degree of symmetry of phases, potentially giving information about the crystallography of a crystal or precipitate and its orientation. However, this distinction is often not made. Thus, conserved and non-conserved phase-field variables can often be found to be respectively termed conserved and non-conserved order parameters [11, 87, 100]. When both conserved and non-conserved variables are employed, they are usually found coupled in the bulk free energy of the system, especially for diffusional transformations.

In the theory suggested by Landau, the Landau theory, a bi-phase system may be defined by the presence of an ordered phase and a disordered phase depending on their degree of symmetry. The coexisting phases are associated with specific values of the non-conserved order parameter ϕ , e.g., traditionally, $\phi = 0$ for the disordered phase and $\phi \neq 0$ for the ordered phase [101]. Depending on the formulation, the phase variable can be arbitrarily defined with different values accounting for the different phases of a system. For example, an unstable disordered phase can be designated by $\phi = 0$ while a stable disordered one is defined by $\phi = -1$ or $+1$ [82]. In [102], $\phi = -1$ accounts for an empty space and $\phi = +1$ denotes a filled space. A one-dimensional example of the variation of a phase-field variable through an diffuse interface is illustrated in Figure 6b. Therein, phases α and β are associated

with $\phi = -1$ and $\phi = 1$ respectively, while the interface is described by the intermediate values of the phase-field variable.

The conserved phase-field quantity is usually a scalar, but the non-conserved variable can be employed as a vector. When used as a scalar, it can be considered a spatial average of its vector form [11]. It is common to use the components of the non-conserved order parameter vector to represent the crystallography and orientation of the phases [103, 104]. Nevertheless, several non-conserved phase-field components can also be used to account for the transitions between the phases in a multi-phase system.

4.2 Minimization of the free energy of a system

4.2.1 The total free energy

In nature, systems strive to find equilibrium by minimizing their energy. In phase-field theory, the evolution of a microstructure, e.g. a phase transformation, is governed by kinetic equations based on the minimization of the total free energy \mathcal{F} . The total free energy of the system can be expressed as the sum of characteristic free energies, which are functions of time, space, pressure, temperature and the phase-field variables. The total energy commonly boils down to

$$\mathcal{F} = \iiint \psi dV = \mathcal{F}_{bulk} + \mathcal{F}_{grad} + \mathcal{F}_{el} + \dots, \quad (19)$$

where $\mathcal{F}_{bulk} = \iiint \psi_{bulk} dV$ is the bulk or chemical free energy and V is the volume of the system. The bulk free energy density ψ_{bulk} typically takes the form of a double well, which in the Landau theory is called Landau potential or Landau free energy density. The gradient free energy \mathcal{F}_{grad} is related to the interfacial energy and accounts for the presence of interfaces through Laplacian terms. The bulk free energy and gradient free energy can be regrouped in a single term, the structural free energy \mathcal{F}_{str} [105]. The elastic-strain free energy \mathcal{F}_{el} represents the energy stored by a system subjected to stresses or undergoing elastic deformation. The energy associated with a microstructural swelling or dilatation due to phase transformation can be reflected in the elastic-strain energy term as in [82] or in an extra energy term, e.g. the interaction energy in [106]. Finally, other free energy terms can be added to the expression, such as free energies related to electrostatics and magnetism. Generally, in phase-field modeling, \mathcal{F} is employed to characterize the thermodynamic properties of a system and it is not systematically specified as Gibbs or Helmholtz free energy [82].

4.2.2 The bulk free energy density

Originally, the Landau theory was developed to describe phase transformations at a critical temperature T_c through the use of a thermodynamic potential, the Landau potential. The latter can be written in terms of pressure P , temperature T and an order parameter ϕ (or a combination of several order parameters reflecting the symmetry relations between the phases). It was suggested by Landau that it can be formulated as a polynomial expansion in power of ϕ as [101],

$$\psi_{bulk}(P, T, \phi) = \psi_{bulk}(P, T, \phi = 0) + \sum_{n=1}^N \frac{D_n(P, T)}{n} \phi^n, \quad (20)$$

where D_n denotes the n^{th} coefficient of the phase-field variable or order parameter and can be a function of pressure and temperature. In this paper, the pressure P is assumed constant in all descriptions. For the case of Landau's theory, it is assumed that $D_2 = a_0(T - T_c)$ where a_0 is a phenomenological positive constant, T is the material temperature and T_c is the phase transition temperature. The Landau free energy can be chosen to be symmetric, for instance, in case of a simple bi-phase system characterized by a symmetric phase diagram, but can also be non-symmetric, for example, in case of a gas-liquid transition or system with a phase diagram including a critical point [11].

When using a fourth-order Landau potential with $D_1 = D_3 = 0$, $D_2 \neq 0$ and $D_4 > 0$, the stability of the solid solution, the disordered phase, is traditionally defined by the zero root of the derivative of the system's total free energy density, while its non-zeros roots characterize the stability of the second phase, the ordered phase. By solely considering the bulk free energy in the total free energy of the system, the prevailing phase is that for which the order parameter values minimize the Landau potential. Thus, in material regions, where the total free energy of the system is similar to that depicted in Figure 7a, the solid solution is stable while the second phase is unstable since there is only one minimum, i.e. for $\phi = 0$. Figure 7b describes a situation where the second phase is stable and is expected to develop while the matrix phase, unstable, should disappear, i.e. for $\phi \neq 0$. With Landau's formulation, Figure 7a illustrates the appearance of the Landau potential for $T > T_c$, i.e. $D_2 > 0$. The situation displayed in Figure 7b corresponds to an undercooling of a pure solid solution as $T < T_c$, i.e. $D_2 < 0$. Thus, the variation of the material temperature can modify the profile of the Landau potential.

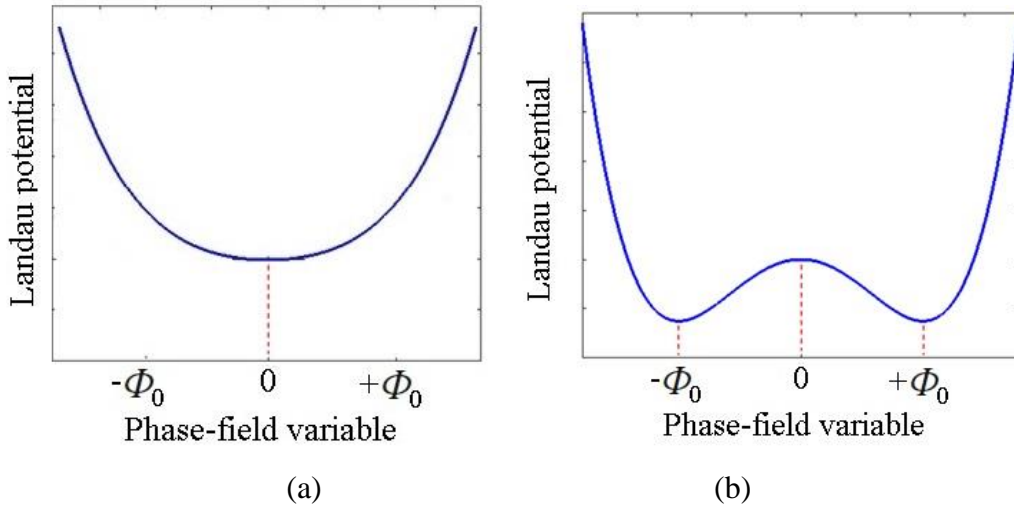


Figure 7 : Example of a Landau potential profile with (a) $T > T_c$ and (b) $T < T_c$.

For constant material temperature, the second phase precipitation can be triggered by energy contribution other than \mathcal{F}_{str} . In [107], the stress induced by a dislocation, which has an active role in the microstructure evolution, is taken into account by including the elastic-strain free

energy into the total free energy of the system. The gradient of stress in the proximity of the dislocation induces an increase of the transition temperature such that the total free energy density profile changes with distance from the flaw. Thus, second-phase formation can occur in the vicinity of the dislocation, where $T < T_c$. Away from the defect, $T > T_c$ and, therefore, the solid solution remains stable. The shift of the transition temperature causes a modification of the total free energy density profile as that illustrated in Figure 8a for a symmetric sixth-order Landau potential.

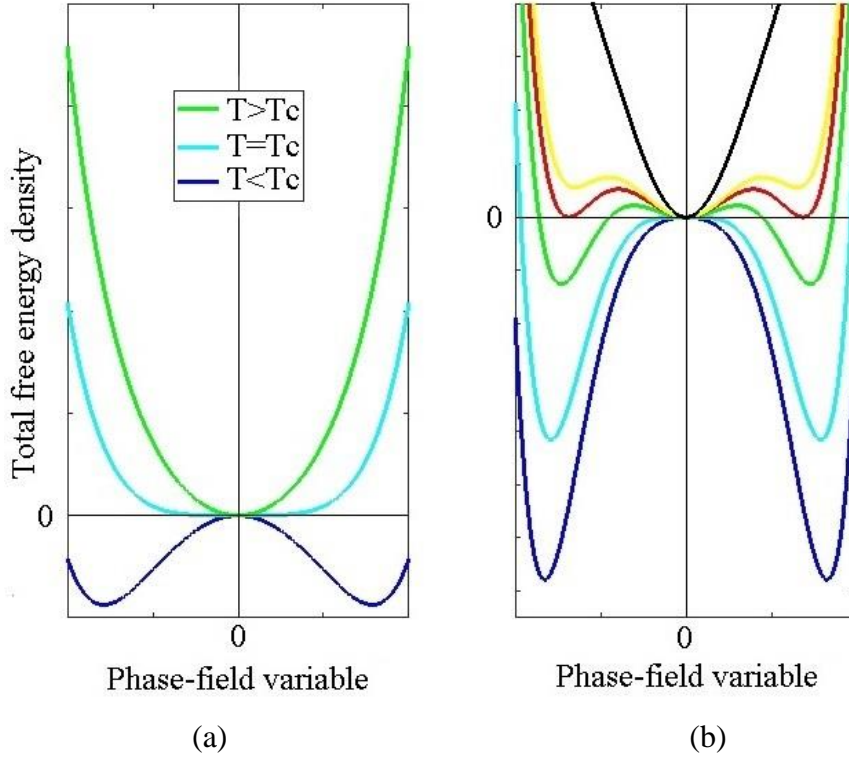


Figure 8 : Total free energy of a system omitting the gradient term and including a symmetric 6th order Landau potential to capture. (a) second-order transitions ($D_4 > 0$), and (b) first-order transitions ($D_4 < 0$).

In other phase-field formulations, the bulk free energy density can be written as in Eq. (20), where the coefficients D_n are constant. A typical example of a fourth-order Landau polynomial with $D_4 > 0$ is

$$\psi_{bulk} = p \left(-\frac{1}{2} \phi^2 + \frac{1}{4} \phi^4 \right), \quad (21)$$

where $p/4$ is the height of the double well or nucleation energy barrier, which needs to be overcome to allow phase transformation [82], and ϕ is a scalar phase-field variable. With this example, $\phi = -1$ and $\phi = 1$, the minima of the function, can be chosen to represent the existence and stability of two distinct material phases, e.g. the metallic solid solution and a second phase. In absence of \mathcal{F}_{grad} , the total free energy density of a system defined in this manner has a double-well shape, as illustrated in Figure 9a-b. In the situation depicted by the Figure 9a, the total free energy density of the system is symmetric, i.e. the minima have the same values, and, therefore, both phases can coexist in the microstructure. Figure 9b presents

a situation, where the global minimum is obtained for $\phi = 1$ and indicating the prevalence of the second phase over the solid solution. The domination of the matrix phase and the second phase over one another can also be caused by the addition of non-symmetric energy terms in the total free energy functional. For example, in [102], the elastic-strain energy includes first and third order terms, which modify the double-well shape by breaking its symmetry.

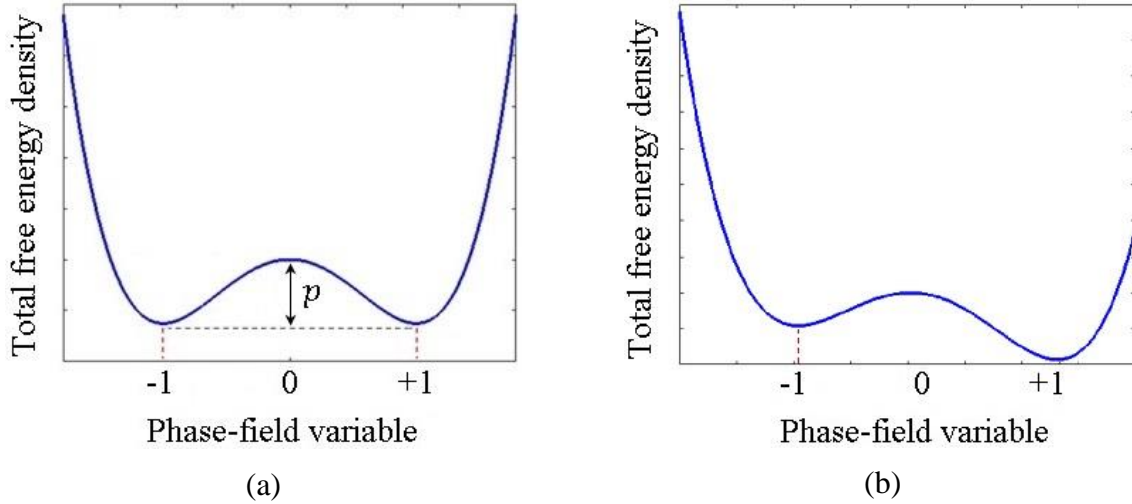


Figure 9 : Example of the total free energy density of a system, (a) where the solid solution and the precipitate can coexist, and (b) where the second-phase prevails over the matrix phase. The gradient free energy density term is neglected.

4.2.3 First- and second-order transitions

First-order transitions are characterized by a discontinuous derivative of the system free energy with respect to a thermodynamic variable and a release of latent energy and nucleation of a metastable state of the matter is its starting point. In addition, some materials, which undergo such type of transformation, can display a coexistence of multiple phases for many thermodynamic conditions and compositions. Transformation examples such as liquid solidification and vapor condensation are part of the first-order transition category. When analyzing the total free energy density of a system with respect to the phase field variables or order parameters, metastability is indicated by local minima, while stability is represented by global minima. For second-order transitions, the system free energy first derivative is continuous with no release of latent heat with the second derivative of the system free energy of the system being discontinuous. In this case, the transformation is triggered by the presence of thermal fluctuations. This category includes phenomena such as phase separation of binary solutions, spinodal decomposition in metal alloys or spontaneous ferromagnetic magnetization of iron below the Curie temperature [11].

Depending on the formulations, the use of a fourth-order Landau expansion can allow to capture either first- or second-order transformation [108]. Double-well potentials expressed as in Eq. (20) with $D_4 > 0$ and Eq. (21), are suitable to modeled first-order transition when non-symmetric terms are added, see Figure 9. It is also possible to utilize a symmetric fourth-order polynomial defined as in the Landau theory to capture first-order transition by taking $D_4 < 0$. But, in this case the use of the formulation is limited since the Landau potential is unbounded.

The addition of higher order terms is necessary to overcome this limitation. Second-order phase transformations are commonly accounted for by using a symmetric fourth-order Landau potential, as defined in Landau theory with $D_4 > 0$, see Figure 7. Both order transitions can be modeled by using a higher-order Landau potential as in [107], where a symmetric sixth-order polynomial is employed, with $D_1 = 0$, $D_3 = 0$ and $D_5 = 0$ considering Eq. (20). A system free energy density, which includes such a sixth-order free energy density, is presented in Figure 8a and Figure 8b. In this case, $D_6 > 0$, which ensures the stability of the system, $\phi = 0$ designates the disordered phase and $\phi \neq 0$ represents the ordered phase. First-order transformations are regarded when $D_4 < 0$ while second-order transitions are considered for $D_4 > 0$. In Figure 8a and Figure 8b, the lower the curves the larger the material transition temperature or the lower the material temperature. With this formulation, both phases may coexist when the minima of the system's total free energy have the same value. For example, this can occur for $D_4 < 0$, as displayed by the red curve in Figure 8b.

4.2.4 Multi-phase and multi-order-phase systems

In order to account for the energy of a multi-phase system, the bulk free energy density can be constructed with more phase-field variables or components than in the formulations presented above. Thus, various aspects and quantities such as the concentration of solute, the existence of phases, their crystallography and orientation can be represented [82]. For example, the evolution of a multi-phase microstructure can depend on the variation of the concentration of N components (c_1, c_2, \dots, c_N) and on the degree of symmetry of the different phases represented by P non-conserved order parameters ($\eta_1, \eta_2, \dots, \eta_P$). As the amount of considered phases-field variables increases, the number of kinetics equation to be solved and their complexity increases. Thus, more computational resources are required to capture the evolution of multi-phase systems.

4.2.5 The kinetic equations

The evolution of the microstructure is steered by kinetic equations, as mentioned in section 4.2.1. The Cahn-Hilliard (CH) equation is employed to govern the evolution of conserved phase-field variables [109] while the time-dependent Ginzburg-Landau (TDGL) equation, also known as Allen-Cahn equation [110], is commonly utilized to model the evolution of non-conserved phase-field variables. In this framework, the time derivative of a phase-field component is connected to the functional derivative of the total free energy of the system with respect to the same phase-field component and a positive kinetic coefficient. The latter is usually referred to as the diffusion coefficient in case of the CH equation and mobility coefficient for the TDGL equation. Through this formulation, the kinetic equations minimize the total free energy of the system at all times, and consequently, allow modeling the dynamic evolution of the microstructure towards a state of equilibrium [111]. When multi-component phase-field variables are employed and thermal fluctuations are neglected, the TDGL and the CH equations can be respectively written with tensor notations as

$$\frac{\partial \eta_i}{\partial t} = -M_{ij} \frac{\delta \mathcal{F}}{\delta \eta_j}, \quad (22)$$

and

$$\frac{\partial \psi_i}{\partial t} = \nabla \cdot \left(L_{ij} \nabla \frac{\delta \mathcal{F}}{\delta \psi_j} \right), \quad (23)$$

where the parameters L_{ij} and M_{ij} respectively denote the matrices of diffusion and mobility coefficients. When considering quasi-static transformation, the system is in equilibrium. This state is modeled by setting the functional derivative of the system's total free energy with respect to the phase-field variables to zero.

Phase-field theory, as introduced in the current section, is used to build the models presented in the next sections of the thesis. Three of them are applied to crack-induced precipitation by using LEFM, introduced in section 3.

5 Phase-field models to predict stress-induced precipitation kinetics

Over the years, models have been developed to study, predict and simulate second-phase nucleation and formation in materials [104, 106, 112, 113, 114, 115, 116, 117, 118]. Some of them are based on PFT and have found applications in hydride formation modeling in a context of HE. Phase-field methods continue being used increasingly for phase precipitation modeling.

Models based on a symmetric fourth-order Landau-type potential cannot always suitably represent first- and second-order phase transitions. In contrast, microstructure changes involving these two types of phase transformation can be conveniently modeled through the use of higher-order polynomials. A symmetric sixth-order Landau potential-based model was presented in [105, 107] and found suitable to study crack- and dislocation-induced second-phase formation. Such models can be used to cost-effectively study precipitation kinetics by taking into account multiple transitions orders without changing the overall formulation. As seen in sections 2.2.4 and 2.2.5, second/third-phase formation can be triggered and enhanced at the grain/phase boundary and in presence of stress concentrators such as opening cracks in a number of materials. The combination of these aspects on precipitation kinetics might be difficult to observe in laboratory. Modeling is a practical and cheap route to study the phenomenon. However, the addition of multiple aspects affecting the microstructure into a formulation can increase its complexity and, consequently, the computational resources required to solve considered situations as highlighted in [104]. Optimization of such formulation, e.g. by the reduction of the number of equations to be solved, can be beneficial in industrial engineering project in terms of time and costs. Additionally, the coupled mechanical and the phase-field aspects of the microstructural evolution are often treated separately and with different computer programs. By using fully coupled methods convergence can be obtained robustly and both aspects can be considered simultaneously [119]. The possibility to use a single mechanical commercial program to account for interdependent multi-physical aspects affecting second-phase formation can be more interesting within industrial engineering considering cost and time efficiency.

In this thesis, for its practicality to model complex microstructures, PFT is chosen to model stress-induced precipitation kinetics. Different approaches are presented to account for the different aspects related to the system configuration and complexity. All models account for stress-induced precipitation driven by the coupling of the phase transformation-induced swelling of the system and the stress. Model 1 is based on Massih and Bjerken's work [105, 107], in which a scalar structural order parameter is employed. This model is used to study defect-induced second-phase precipitation within a crystal for different sets of sixth-order Landau potential coefficients. The near-crack stress is implicitly incorporated in the mathematical formulation through the use of LEFM relations for isotropic and anisotropic materials. The second and third models have been developed in order to capture stress-induced second- and third-phase precipitation at grain/phase boundaries, by employing a two-component non-conserved phase-field variables and for a uniform and constant concentration of solute. This choice has been made in order to account for phase transformation in

polycrystalline and multi-phase microstructures, e.g. hydride formation occurring preferentially along grain and phase boundaries in a Ti64 microstructure. These models are suited to predict intragranular, intergranular and interphase crack-induced precipitation as LEFM applied to interface cracks is employed and a parameter is introduced to account for the energy of the grain/phase boundary. Anisotropy in terms of elastic constants and dilatation of the system during phase transformation can also be considered with models 2 and 3. With models 1-3, only the phase-field equation needs to be solved numerically as the mechanical equilibrium is taken into account analytically. This allows modelling of second or third-phase precipitation kinetics with numerical efficiency. Model 4 is formulated to model second-phase formation induced by stress by considering a fourth-order double-well and a non-conserved phase-field scalar. With this formulation, the orientation of the forming hydrides perpendicular to the applied stress as mentioned in section 2.2.2 is captured. The numerical approach associated with this model is based on FEM and a fully coupled method by using the commercial program Abaqus. In this thesis, only diffusionless transformations are considered in an early stage of second/third phase formation as diffusional phase changes induced by stress are assumed to be slower for a given concentration of solute. Thus, the phase transformation aspect is accounted for by solely employing the TDGL equation with all models while mechanical equilibrium is represented either analytically or numerically. Furthermore, the same elastic constants are considered for the precipitate and the matrix phase the second-phase forms from for all models for simplicity.

This section gives a description of the models and numerical strategies used in this thesis.

5.1 Model 1: Sixth order Landau potential for crack-induced second-phase formation modeling

In model 1, 2 and 3, the spatial position of a particle can equally be referred to through a Cartesian or a polar coordinate system. Thus, the position vector x_i is either defined by (x_1, x_2, x_3) or (r, θ, z) . In model 1, second-phase precipitation near the tip of a crack opening in mode I in a crystal is considered. The origin is chosen to be located at the crack tip as presented in Figure 10.

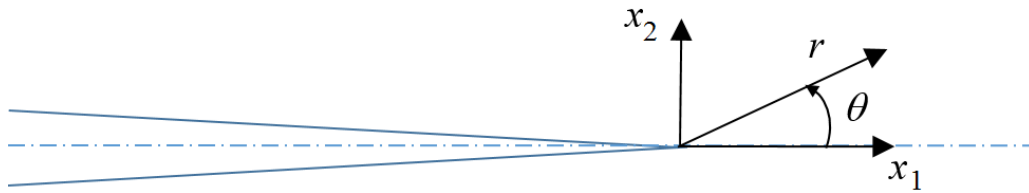


Figure 10: Geometry of the system.

In model 1, employed in papers A and B, a non-conserved order-parameter scalar η is chosen to describe the evolution of the microstructure such that $\eta = 0$ designates the matrix or the solid solution and $\eta \neq 0$ represents for the second phase.

The total free energy density of the system with a volume V is derived from Eq. (19) and becomes

$$\mathcal{F} = \iiint_V \left[\frac{g}{2} (\nabla \eta)^2 + \psi_{bulk}(\eta) + \frac{1}{2} \sigma_{ij} \varepsilon_{ij}^{el} - \xi \eta^2 \varepsilon_{ll} \right] dV, \quad (24)$$

where the sum of the first two terms on the right hand side is equal to the structural free energy \mathcal{F}_{str} , the third term is the elastic-strain energy and the last term represents the interaction energy \mathcal{F}_{int} . The positive coefficient g is related to the interfacial energy and the interface thickness. The dilatation of the system caused by lattice misfit during phase transformation is represented by \mathcal{F}_{int} and includes a positive constant ξ , called striction factor, which is related to the lattice constant [120, 121]. The tensor quantities σ_{ij} , ε_{ij} and u_i respectively accounts for the stress tensor, the strain tensor and the displacement field. The sixth-order Landau potential ψ is expressed as

$$\psi_{bulk}(\eta) = \frac{1}{2} \alpha_0 \eta^2 + \frac{1}{4} \beta_0 \eta^4 + \frac{1}{6} \gamma \eta^6, \quad (25)$$

Where the phenomenological parameters α_0 , β_0 and γ are constants related to temperature and the stability of the system is ensured by imposing $\gamma > 0$, as mentioned in section 4.2.3. It is assumed that the system is at mechanical equilibrium at all times, which yields:

$$\frac{\partial \sigma_{ij}}{\partial x_j} = \frac{\partial}{\partial x_j} \left(\frac{\delta \mathcal{F}}{\delta \varepsilon_{ij}} \right) = Q_i, \quad (26)$$

where Q_j represents the crack-induced force field. Proceeding as in [122] for an isotropic body and by using Eq. (3), Eq. (26) can be rewritten as

$$M \frac{\partial u_i}{\partial x_j \partial x_j} + (\Lambda - M) \frac{\partial^2 u_l}{\partial x_i \partial x_l} - \xi \frac{\partial (\eta^2)}{\partial x_i} = M \Omega_i(x_i), \quad (27)$$

where u_i is the displacement field, Ω_i accounts for the variation in strain field induced by the opening crack tip, and M and Λ denote the shear and the P-wave moduli respectively. Equation (27) is analytically solved for an isotropic body in order to determine $\varepsilon_{ll} = \partial u_l / \partial x_l$ as function of the order parameter and eliminate the elastic field from Eq. (24) as explained in [106]. Therefore, the total energy of the system for constant pressure can be given as a function of the order parameter solely. It can be expressed as

$$\mathcal{F}(\eta, T) = \mathcal{F}(0, T) + \iiint_V \left[\frac{g}{2} \nabla^2 \eta + \frac{1}{2} \alpha \eta^2 + \frac{1}{4} \beta \eta^4 + \frac{1}{6} \gamma \eta^6 \right] dV, \quad (28)$$

where $\mathcal{F}(0, T)$ is an energy that depends on temperature and stress, while α and β are the Landau potential coefficient of the quadratic and the quartic terms of η , which depend on the crack displacement field. Thus, in plane strain conditions and through the use of LEFM,

$$\alpha \equiv |\alpha_0| \left(\text{sgn}(\alpha_0) - \sqrt{\frac{r_0}{r}} f(\theta, \zeta) \right), \quad (29)$$

where sgn is the sign function and $f(\theta) = \frac{1}{2S_{11}}[A_1 f_{11}(\theta) + A_2 f_{22}(\theta) + A_3 f_{12}(\theta)]$ with $A_1 = S_{11} + S_{12}$, $A_2 = S_{12} + S_{22}$ and $A_3 = S_{16} + S_{26}$. The trigonometric functions f_{ij} are given in Eqs.(4)-(6) for an isotropic system, and in Eqs. (9)-(11) for anisotropic media. The quantities S_{ij} are the planar compliance components calculated for a determined crystal plane.

For isotropic bodies where E and ν account for the Young's modulus and Poisson's ratio respectively, $A_1 = A_2 = (1 + \nu)(1 - 2\nu)/E$, or $1/[2(\Lambda - M)]$, while $A_3 = 0$ and, $S_{11} = (1 + \nu)(1 - \nu)/E$ or $\Lambda/[4M(\Lambda - M)]$. The length parameter r_0 is expressed as

$$r_0 = \frac{8}{\pi} \left(\frac{\xi K_I S_{11}}{|\alpha_0|} \right)^2, \quad (30)$$

where K_I is the stress intensity factor for the mode-I crack. Hence, α is not only temperature dependent, but also space and load dependent. Its temperature dependence can be explicitly formulated as

$$\alpha = a (T - T_c(r, \theta)), \quad (31)$$

where $T_c(r, \theta, \zeta) = T_{c_0} + \frac{4\xi K_I S_{11}}{a} \frac{f(\theta)}{\sqrt{2\pi r}}$ is the phase transition temperature modified by the influence of the crack-induced stress field and T is the material temperature, which is assumed constant. The constant T_{c_0} denotes the phase transition temperature in a defect-free crystal, which is included in the quadratic term of the Landau potential as $\alpha_0 = a[T - T_{c_0}]$. Under defect-free conditions, $T > T_{c_0}$ corresponds to the prevalence of the solid solution and for $T < T_{c_0}$ the second phase becomes stable whereas the solid solution becomes unstable. In presence of a crack, these stability conditions are readjusted by substituting T_{c_0} by $\max(T_{c_0}, T_c)$. Thus, the effect of the space-dependent crack-induced stress field on the solid solubility limit becomes the driving force for the microstructural evolution.

The coefficient of the quartic term of the total free energy, β , is dependent of the elastic constants of the material and, for isotropic bodies, is expressed as

$$\beta = \beta_0 - \frac{2\xi^2}{\Lambda}. \quad (32)$$

When the crack is inclined with an angle ζ relative to crystallographic planes, as illustrated in Figure 11 for an HCP crystal structure, a change of base for the stress tensor is necessary.

Hence, the trigonometric function f is not only dependent of the second polar coordinate θ but also of the crack inclination ζ through A_1 , A_2 and A_3 as

$$A_1(\zeta) = S_{11} \cos^2 \zeta + S_{12} + S_{22} \sin^2 \zeta + \frac{1}{2}(S_{16} + S_{26}) \sin 2\zeta, \quad (33)$$

$$A_2(\zeta) = S_{11}\sin^2 \zeta + S_{12} + S_{22}\cos^2 \zeta - \frac{1}{2}(S_{16} + S_{26}) \sin 2\zeta, \quad (34)$$

$$A_3(\zeta) = (S_{11} - S_{22}) \sin 2\zeta + (S_{16} + S_{26}) \cos 2\zeta. \quad (35)$$

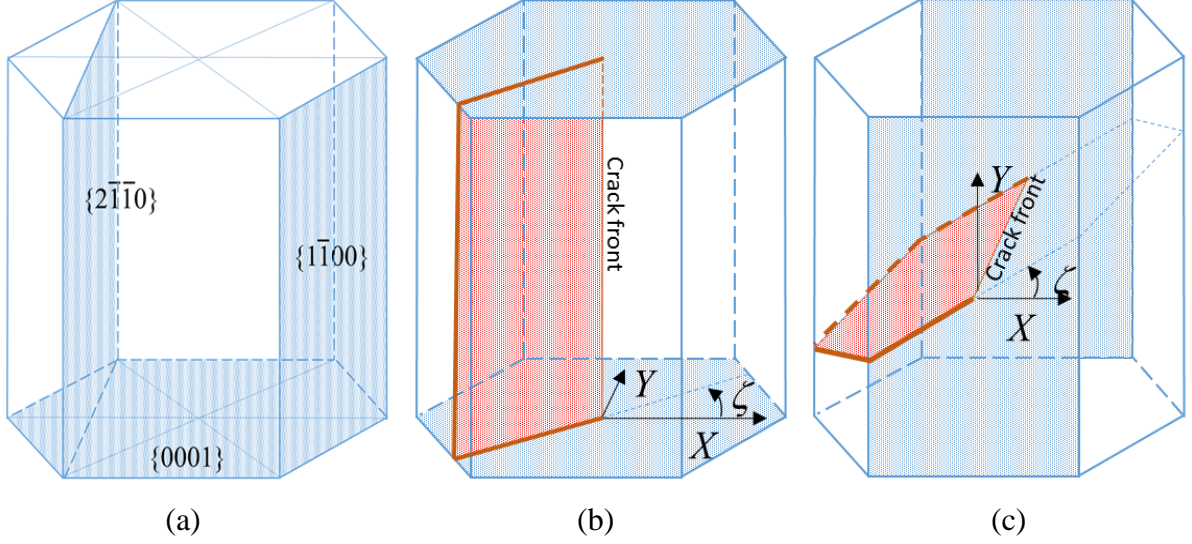


Figure 11: a) Basal and prismatic planes in an HCP crystal. b) Crack plane (in red) orthogonal to the basal planes (in blue) with an inclination angle ζ relative to $\{1\bar{1}00\}$ planes. c) Crack plane (in red) orthogonal to prismatic planes of the $\{1\bar{1}00\}$ family (in blue).

The TDGL equation, presented in Eq. (22), needs to be solved in order to determine the evolution of the structural order parameter and, therefore, predict the possible microstructural changes induced by the presence of a crack in the system. To simplify the numerical treatment, dimensionless coefficients are introduced as, $\eta = \sqrt{\frac{|\alpha_0|}{|\beta|}} \Phi$, $r = \sqrt{\frac{g}{|\alpha_0|}} \rho$,

$x_i = \sqrt{\frac{g}{|\alpha_0|}} \tilde{x}_i$, $r_0 = \sqrt{\frac{g}{|\alpha_0|}} \rho_0$, $t = \frac{1}{|\alpha_0| M_{11}} \tau$ in Eq. (28) so that Eq. (22) becomes

$$\frac{\partial \Phi}{\partial \tau} = \tilde{\nabla}^2 \Phi - (A \Phi + \text{sgn}(\beta) \Phi^3 + \kappa \Phi^5), \quad (36)$$

where $A = \text{sgn}(\alpha_0) - \sqrt{\frac{\rho_0}{\rho}} f(\theta, \zeta)$ and $\tilde{\nabla}$ is the dimensionless gradient operator.

5.2 Models 2 and 3: Stress-induced precipitation at grain/phase boundaries

Models 2 and 3, employed in papers C and D respectively, are formulated such that they account for stress-induced precipitation in polycrystalline and multi-phase systems respectively. Particular attention is paid for configurations where the stress is induced by defects, such as intergranular, interphase and intragranular cracks. The systems represented with model 2 are composed of grains of the same phase but with different orientations. Model

3 is an improved version of model 2, which can represent different phases in the matrix. For these approaches, phase transformation is considered for a given concentration of solute C . Thus, these models are based on the phase-field method and use a two-component non-conserved phase-field variable (η_1, η_2) to represent the microstructure. The formulation of the bulk free energy density is such that these components are allowed to vary from -1 to 1 , where $(-1, -1)$ designates the stability of the solid solution in phase 1, $(-1, 1)$ represents that of the solid solution in phase 2 and $(1, \eta_2)$ denotes the stability of the precipitate. The intermediate values of the phase-field variable represent the interfaces between the different grains and phases. In model 3, phase 1, phase 2 and the phase of the precipitate are referred to as phases α , β and δ respectively. For model 2, the β -phase region designates a second α -phase region but with a different orientation.

The bulk free energy densities used for these models are illustrated in Figure 12 and have been formulated as

$$\psi_{bulk}(\eta_i) = P_0 (f_a f_b + f_c f_d), \quad (37)$$

with

$$f_a = (\eta_1^2 - 1)^2, \quad (38)$$

$$f_b = 1 \text{ for model 2,} \quad (39)$$

$$f_b = -\frac{1}{3} p \eta_2^3 + p \eta_2 + q \text{ for model 3,} \quad (40)$$

$$f_c = (\eta_2^2 - 1)^2, \quad (41)$$

$$f_d = \frac{s}{4} [\eta_1(\eta_1 + 2)(\eta_1^2 + 2\eta_1 - 6) - 7] \text{ for model 2,} \quad (42)$$

$$f_d = a_{\alpha\beta} - s h_{m\delta} \text{ for model 3,} \quad (43)$$

where $h_{m\delta} = \frac{1}{4}(-\eta_1^3 + 3\eta_1 + 2)$ is an interpolation function, which satisfies the relations $h_{m\delta}(-1) = 0$ and $h_{m\delta}(1) = 1$, $p = 3(a_{\beta\delta} - a_{\alpha\delta})/4$ and $q = (a_{\alpha\delta} + a_{\beta\delta})/2$. The phenomenological parameter P_0 is the height of the double well formed by this function and the coefficient $a_{\alpha\delta}$, $a_{\beta\delta}$ and $a_{\alpha\beta}$ are the respective energy barrier coefficients of the α/δ , the β/δ , and the α/β transitions. The phenomenological parameter s has been introduced in these models to account for the energy level of the grain/phase boundary by controlling the nucleation (or activation) energy barrier for the matrix/precipitate transition at the grain/phase boundary. Thus, a reduction of the activation energy barrier within the interface between the matrix phases is modeled by an increase of the value of s . The variation of s allows modeling different types of grain/phase boundaries, i.e. different level of interface incoherency can be represented.

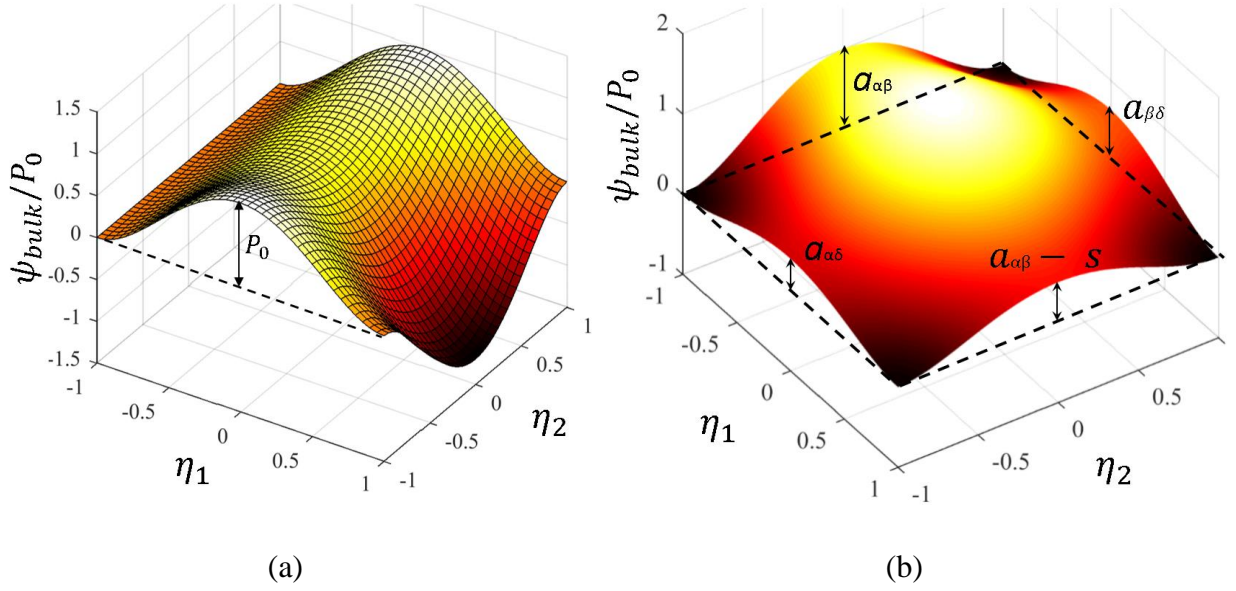


Figure 12: Landau potential normalized with respect to P_0 for (a) model 2 and (b) model 3 with $s > 0$.

The gradient free energy is expressed as $\mathcal{F}_{grad} = \frac{1}{2} \int \{g_{m\delta}(\nabla\eta_1)^2 + g_{\alpha\beta}(\nabla\eta_2)^2\} dV$, where the phenomenological parameters $g_{m\delta}$ and $g_{\alpha\beta}$ are positive constants related to the interfacial energies relative to the interface matrix/hydride and the interface between the matrix regions, grain or crystals respectively [11]. The function $g_{m\delta}$ is a third-degree polynomial in η_2 , which interpolates $g_{\alpha\delta}$ and $g_{\beta\delta}$ over the interface between the matrix phases. With model 2, $g_{\beta\delta} = g_{\alpha\delta}$ since the same phase is considered for the two matrix-phase regions.

The parameters P_0 , $g_{m\delta}$, $g_{\alpha\beta}$, $a_{\alpha\delta}$, $a_{\beta\delta}$ and $a_{\alpha\beta}$ are connected to the specific interfacial energy γ_{ij} and the width w_{ij} of the different interfaces. Proceeding as in [123], the latter quantities can be estimated for a 1d-system at equilibrium, where no elastic-strain energy contribution is considered, as

$$w_{ij} = \alpha_0 \sqrt{\frac{g_{ij}}{2 a_{ij} P_0}}, \quad (44)$$

and

$$\gamma_{ij} = \frac{4}{3} \sqrt{2 a_{ij} g_{ij} P_0}, \quad (45)$$

where $i \in \{\alpha, \beta\}$, $j \in \{\delta, \beta\}$ and $i \neq j$. In order to use these relations with model 2, the coefficient $a_{\alpha\delta}$, $a_{\beta\delta}$ and $a_{\alpha\beta}$ must be set so that $a_{\alpha\delta} = a_{\beta\delta} = a_{\alpha\beta} = 1$.

As introduced in section 4.2.1, the total energy of the system with a volume V is the sum of the bulk free energy, the gradient energy and the elastic-strain energy \mathcal{F}_{el} . The latter energy term is formulated as in [85, 124],

$$\mathcal{F}_{el} = \int \psi_{el} dV = \int \left[\frac{1}{2} \sigma_{ij} \varepsilon_{ij}^{el} - \sigma_{ij}^A \varepsilon_{ij} \right] dV, \quad (46)$$

where σ_{ij} , σ_{ij}^A , ε_{ij}^{el} and ε_{ij} denote the internal stress, the applied stress, the elastic strain and the homogeneous strain tensors respectively. The swelling of the system during phase transformation is taken into account in the total strain ε_{ij}^{tot} , expressed as

$$\varepsilon_{ij}^{tot} = \varepsilon_{ij}^{el} + \varepsilon_{ij}^s Q h_{m\delta}, \quad (47)$$

where ε_{ij}^{el} and ε_{ij}^s denote the elastic-strain and the stress-free strain tensors, respectively, and $h_{m\delta}(\eta_1) = \frac{1}{4}(-\eta_1^3 + 3\eta_1 + 2)$ is an interpolation function, which satisfies the relations $h_{m\delta}(-1) = 0$ and $h_{m\delta}(1) = 1$. The total strain is made dependent on η_l solely through the term $\varepsilon_{ij}^s Q h_{m\delta}$ as ε_{ij}^{el} is assumed independent of η_l . The parameter Q is coupled to the eigenstrains to account for the difference in solubility of solute in the phases of the solid solution during precipitation: $Q = 1$ in model 2 and $Q = C/C_s$ in model 3, where C_s designate the solid solubility limit of solute in absence of applied stress. While C is constant and uniform in the whole system, C_s is interpolated over the interface between the different matrix phases through a similar function as $g_{m\delta}$. Linear elastic properties are assumed for all phases such that the stress tensor is related to the elastic strain tensor through the use of Hooke's law. In paper C and D, all phases are presumed isotropic for simplicity. Nevertheless, models 2 and 3 can also incorporate anisotropic elastic constants. In model 2, the elastic constants of the phase regions are assumed to remain unchanged through the grain boundary. In model 3, since the elastic constants can be different from one matrix phase to the other, they are interpolated over the interface that separates them from each other. In paper C, the stress-free strains are considered isotropic. In this case, they can be written $\varepsilon_{ij}^s = \varepsilon_0 \delta_{ij}$, where ε_0 is a positive constant. Both isotropic and anisotropic transformation-strains are considered in paper D. If the deformation of the system induced by phase transformation is different from one matrix phase to the other, then the eigenstrains are interpolated over the interface between the matrix phases.

In Eq. (46), the applied stress σ_{ij}^A has to be replaced by the analytical expression of the stress field prevailing in the system. In presence of a crack, the stress residing in the proximity of the crack-tip is modeled through the use of LEFM. In paper C, model 2 employs the expression given in Eq. (1) by neglecting the high order terms and considering the trigonometric functions in Eqs. (4)-(6). This is enough to model the stress in the vicinity of cracks lying in grains or along grain boundaries. In order to account for the stresses induced by cracks, including interface cracks, in multi-phase systems, the use of Eq. (14) is made in paper D with model 3. In order to keep continuity of the system, the stress field is interpolated over the interface between the different matrix phases. In absence of applied stress, the elastic-strain free energy is equal to the first term of the right-hand side of Eq. (46). When a stress is applied to the system, the second term of Eq. (46) is non-zero and gives rise to the driving force for precipitation by inducing a shift in the solid solubility limit in the solid solution phases. The applied stress field can be substituted by the expression given in (1) through the use of Eqs. (9)-(11) to represent the near crack-tip stress field in an anisotropic

media as with model 1 when modeling crack-induced precipitation in an HCP crystal. Inclination of a crack in an anisotropic crystal structure can also be taken into account in the same manner as with model 1. Other types of defect-induced stresses can be included in the models, e.g. the expressions for an edge dislocation-induced stress field in [122] can be used for appropriate studies.

In both models, the possible movement of the transition front between the matrix phases is assumed to be much slower than the precipitation of a second or third phase. Consequently, the evolution of the phases, within the time scale of precipitation, can be obtained by solely numerically solving the TDGL equation for η_1 as in Eq. (22), which, in models 2 and 3, can also be written

$$\frac{\partial \eta_1}{\partial \tau} = g_{m\delta} \nabla^2 \eta_1 - \left(\frac{\partial \psi_{bulk}}{\partial \eta_1} + \frac{\partial \psi_{el}}{\partial \eta_1} \right), \quad (48)$$

where $\tau = M_{11} t$, in which M_{11} is the mobility coefficient and t is the time.

5.3 Model 4: Stress-induced second-phase formation modelling applied to commercial software

The fourth model accounts for stress-induced second-phase formation and is part of a numerical methodology, where mechanical equilibrium and phase-field equations are coupled and solved concurrently. A non-conserved phase-field scalar φ is selected to describe the evolution of the phases. It is defined so that $\varphi = -1$ characterizes the prevalence of the solid solution, and $\varphi = 1$ corresponds to the second-phase dominance.

Here, the total energy of the system with a volume V is the sum of the bulk free energy, which includes the same fourth-order Landau potential as that given in Eq. (21), the gradient free energy $\mathcal{F}_{grad} = \int \frac{g}{2} (\nabla \varphi)^2 dV$ and the elastic-strain energy \mathcal{F}_{el} as introduced in section 4.2.1. The misfit of the second phase with the parent phase induces a deformation of the material and is taken into account through the stress-free strain ε_{ij}^s in the total strain ε_{ij}^{tot} similarly to model 2 and 3 as

$$\varepsilon_{ij}^{tot} = \varepsilon_{ij}^{el} + \varepsilon_{ij}^s h(\varphi), \quad (49)$$

where $h(\varphi) = \frac{1}{4}(-\varphi^3 + 3\varphi + 2)$. In the solid solution, $h(-1) = 0$, and in the hydride phase $h(1) = 1$. The energy release in form of material dilatation during phase transformation is embedded in the elastic-strain free energy. Thus, the functional derivative of the latter with respect to the phase field variable can be formulated as

$$\frac{\delta \mathcal{F}_{el}}{\delta \varphi} = -\frac{3}{4} \varepsilon_{ij}^{tot} C_{ijkl} \varepsilon_{kl}^s (1 - \varphi^2). \quad (50)$$

The stress-free strain can be either isotropic or anisotropic and the components, $\varepsilon_{11}^{s'}$ and $\varepsilon_{22}^{s'}$, written in the coordinate system of the crystal structure, i.e. for which the tensor is diagonal,

are set in the directions of the principal stress σ'_{11} and σ'_{22} . The swelling and stress tensors, ε_{ij}^s and σ_{ij} , written in the global coordinate system, are related to $\varepsilon_{ij}^{s'}$ and σ_{ij}' respectively through $\varepsilon_{pq}^{s'} = Q_{ip}^s Q_{jq}^s \varepsilon_{ij}^s$ and $\sigma_{ij}' = Q_{ip}^s Q_{jq}^s \sigma_{ij}$, where Q_{ip}^s and Q_{jp}^s are basis rotation matrices. The components of $\varepsilon_{ij}^{s'}$ are directly provided from the literature, e.g. [32] for Zr-hydrides, and, σ'_{11} and σ'_{22} are the eigenvalues of σ_{ij} .

The problem is driven by the minimization of the energy as the mechanical equilibrium is satisfied at all times. The governing equations are, therefore, the second law of Newton for static equilibrium and the TDGL equation, Eq. (22). By differentiating the different energy terms with respect to φ , the latter becomes

$$\frac{1}{M_{11}} \frac{\partial \varphi}{\partial t} = - \left[\left(-\frac{3}{4} \varepsilon_{ij}^{tot} C_{ijkl} \varepsilon_{kl}^s - p\varphi \right) (1 - \varphi^2) - g \nabla^2 \varphi \right], \quad (51)$$

where M_{11} is the mobility coefficient.

5.4 Summary and comparison of the main features of the models when applied to crack-induced precipitation

The main characteristics and capabilities of the phase-field models for stress-induced precipitation as they are presented in the appended papers are given in Table 1.

Table 1: Characteristics and potentialities of the models.

Paper name	Paper A	Paper B	Paper C	Paper D	Paper E
Model #	1	1	2	3	4
Transition order	first or second	first	first	first	first
Phase-field Components	1	1	2	2	1
Landau-type potential order	sixth	sixth	eighth	seventh	fourth
Elastic property	isotropic	anisotropic (HCP)	isotropic*	isotropic*	isotropic/anisotropic
Stress-free strain	isotropic	isotropic	isotropic	isotropic/anisotropic	isotropic/anisotropic
Number of matrix phases	1	1	1	2	1
Inclusion of stress	implicit	implicit	implicit	implicit	explicit
Crack type	intragranular**	intragranular**	intra/inter-granular	intra/intergranular or interphase	—***
Phase /Grain boundary energy control	no	no	yes	yes	no

*In paper C and D, isotropic elastic constants are employed. Nevertheless, anisotropic elastic constants can also be used. If a near crack-tip stress field is considered in an anisotropic media, LEFM through the use of Eqs. (1) and (9)-(11) can be utilized as in paper B with model 1.

** Model 1 could represent intergranular cracks since the LEFM expressions to be used are the same a crack between two grains of same phase as for an intragranular crack. However, the results might be less realistic with model 1 than with model 2 or 3 since the effect of the grain boundary energy is not captured with model 1.

*** Model 4 is not employed to represent crack-induced precipitation in paper E. Nonetheless, it can be applied on configurations including stress concentrators.

5.5 Numerical solution strategies and boundary conditions

5.5.1 Model 1, 2 and 3

The simulations of the stress-induced precipitation based on model 1, 2 and 3 are performed through the use of the software FiPy [125]. With this Python-based module, the TDGL equation is solved based on a standard FVM over a grid composed of equally sized square elements. The chosen solver employs a LU-factorization solving algorithm. In paper A-D, the applied stress/strain is that of a near crack tip, modeled by Eqs. (1) and (14) depending on the crack configuration.

In the simulations, the element size and time step $\Delta\tau$ are chosen to be small enough to ensure the stability of the solutions [11]. For instance, with model 2 and 3, $\Delta\tau < l^2 / (4 g_{m\delta})$, where l is the element size. During the selection of the element sizes and time steps, convergence studies have also been performed to ensure that the relative error is small, e.g. minor to 4% in paper D.

At the boundary, the condition $\mathbf{n} \cdot \nabla \eta_1 = 0$, where \mathbf{n} is a unit vector perpendicular to the domain limits, is satisfied suggesting symmetry of the phase-field variable value across the boundary. The domain is considered large enough so that it prevents edge effects on the results.

Initially, no precipitate is present in the system in paper A, B and C. Instead, a random distribution of the phase-field variable is made on the computational domain in order to numerically initiate the microstructural change. Physically, this distribution can be interpreted by a thermal fluctuating noise, which can, for instance, trigger phase transformation in metastable systems. In fact, without any initialization the microstructure remains unchanged since the motion of the interfaces is driven by the gradient of the phase-field variable. In paper A, B and D, the range of initial values for the phase-field variable is taken small enough not to affect the results of precipitation kinetics. In paper C, this range is chosen to account for the initial thermal noise but also the presence of solute. In paper D, an initial nucleus is considered centered on the crack tip.

As mentioned earlier, the TDGL equation only is solved for models 1-3. It is solved for η_1 only with model 2 and 3 such that phase transformation between the matrix phases is disregarded. Phase transformation is modeled in predefined configurations of the solid-solution phases. In paper C and D, these phases are represented, as in Figure 5, by distributing the values of the second phase-field component over the mesh through the relation

$\eta_2(y) = \tanh(y \sqrt{2 a_{\alpha\beta} P_0 / g_{\alpha\beta}})$. In particular, this function ensures a smooth transition between the two half parts of the computing domain. For the cases including an interface crack, the parameter s , present in Eq. (37) is set to 0 behind the crack tip because of the material discontinuity. This is done by using the relation $s = s_0 \{\tanh [(x - x_0)/l_{sub}] + 1\}/2$, where s_0 is such that $s = s_0$ for $x > 0$, for x_0 being the abscissa of the crack tip and l_{sub} is set as a sub-atomic length.

5.5.2 Model 4

For model 4, FEM associated to a fully coupled solving method is employed to solve the strongly coupled mechanical-phase field problem. The choice of using a fully coupled method is made as this type of approach is usually more robust than a segregated approach in terms of convergence, especially when the coupled aspects are strongly coupled [119]. The model is integrated into the software Abaqus [14] by using user subroutines, where the fully coupled thermo-mechanical problem is modified and adapted for phase-field modeling. Although the equations relative to mechanical equilibrium are solved numerically, this numerical method offers more flexibility, e.g. in terms of the application of boundary conditions and anisotropy.

Equation (51) undergoes a backward-difference scheme and the solution of the non-linear system is obtained through the use of Newton-Raphson's method, which includes a non-symmetric Jacobian matrix, as

$$\begin{bmatrix} K_{uu} & K_{u\varphi} \\ K_{\varphi u} & K_{\varphi\varphi} \end{bmatrix} \begin{bmatrix} \nabla u \\ \nabla \varphi \end{bmatrix} = \begin{bmatrix} R_u \\ R_\varphi \end{bmatrix}, \quad (52)$$

where ∇u and $\nabla \varphi$ are the correction for incremental displacement and order parameter, K_{ij} are the stiffness sub-matrices of the Jacobian matrix and R_i are the residual vectors for the mechanical and the phase-field aspects of the system.

The numerical approach is applied to a defect-free medium and a notched body with isotropic elastic properties corresponding to zirconium. The quadratic element size is chosen such that the interfaces are well-represented, and an adaptive time increment is employed. The initial seedings is a random distribution of the phase field parameter value. A displacement rate is applied on two opposite ends of the medium, while the other edges are mechanically free. A zero-gradient of the order parameter is also applied on the boundary of both bodies.

6 Summary of the appended papers

The attached papers describe models 1-4 as well as their associated numerical procedures. Simulations were performed for specific situations with all models and the results are presented in this section.

6.1 Paper A

In the first paper, model 1 is applied to isotropic bodies at a temperature T . A parametric study is achieved and illustrates different situations of second-phase formation within a near crack-tip stress field. The influence of the system total free energy coefficients, presented in Eq. (28), on the solution of Eq. (36), and the modification, or shift, of the phase transition temperature by the crack-induced stress gradient are thoroughly discussed.

6.1.1 The analytical steady-state solution

First, Eq. (36) is analytically examined for a steady state and for the condition that the variation of the order parameter in one point does not affect its neighbors, i.e. $\partial\Phi/\partial\tau = 0$ and $\tilde{\nabla}^2\Phi = 0$. One result of this investigation is the phase diagram, illustrated in Figure 13, which exhibits the dimensionless distance from the crack tip versus $\kappa \operatorname{sgn}(\beta)$ for $\alpha_0 > 0$ or $T > T_{c0}$, i.e. for cases where no phase transformation is expected if the system is free from defects.

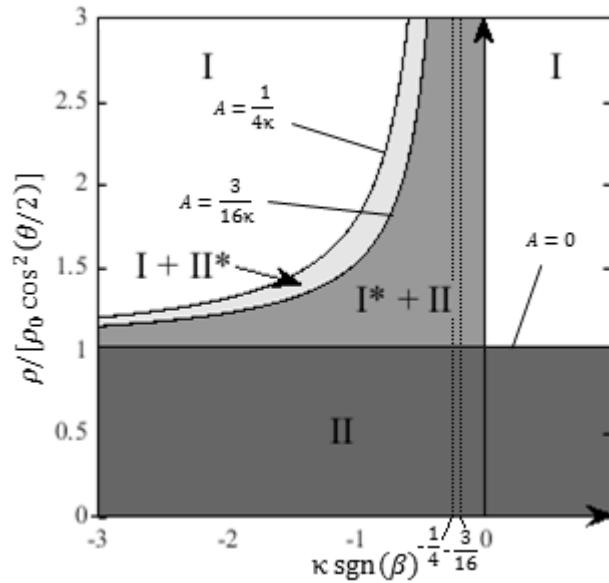


Figure 13: Phase diagram at steady state for $\alpha_0 > 0$ and excluding the gradient free energy term. The notations I and II denote respectively the solid solution and the second phase. The superscript (*) indicates a metastable state of the considered phase.

This phase diagram is useful to approximately predict the steady-state microstructure in presence of a sharp crack when $T > T_{c0}$. Depending on the value of κ , the distance from the crack tip and the sign of β , the second phase may form. Approaching the crack-tip, the modified phase transition temperature T_c is increased, inducing a decrease of α . Thus, this type of quench of the solid solution in the vicinity of the crack tip potentially allows phase

transformation. In addition, the analytical solution predicts first-order transformations for $\kappa \operatorname{sgn}(\beta) < 0$ and second-order transitions for $\kappa \operatorname{sgn}(\beta) > 0$.

For the case of negative β , when $\kappa > 1/4$, four regions are expected to be seen depending on the distance from the crack tip: II, I*+II, I+II* and I. For $\kappa < 1/4$, the analytical solution of Eq. (36) predicts that the furthest region from the crack tip can contain metastable second phase and stable solid solution. For $\kappa < 3/16$, the solid solution is never expected to be stable regardless of the distance from the crack. In case of positive β , two different regions are likely to co-exist depending on the distance from the crack tip. A stable second phase (II) should spontaneously form in the areas close to the crack tip for a length ratio $\rho/\left[\rho_0 \cos^2 \frac{\theta}{2}\right] < 1$ and this region is expected to be surrounded by stable solid solution (I). This inequality represents the transition line between region II and I*+II for negative β . According to the model predictions, for $T < T_{c_0}$ or $\alpha_0 < 0$, the whole considered body is expected to transform into a stable second phase.

6.1.2 Numerical results

The full solution of Eq. (36) applied to the situations analytically investigated in the previous section at steady states is numerically examined and presented in this section.

In all studied cases, the order parameter growth pattern is similar: a relatively sharp peak emerges in the first elements near the crack tip before it reaches a maximum Φ_{max} . At this point, lower values of the order parameter spread around the crack tip as a result of the driving force emanating from the space-dependent phase transition temperature T_c . In other words, the second phase nucleates in the crack-tip closest region and the phase transformation expands with space as long as the condition $T < T_c$ is satisfied. This pattern is sequentially illustrated in Figure 14.

Depending on the value of κ , and the sign of α_0 and β some characteristic data are collected: (i) the peak value of the order parameter, (ii) the time τ_{mp} to reach it, (iii) the steady-state distance between the crack tip to the limit of the second-phase precipitate w_{ss}/ρ_0 for $\tilde{y}/\rho_0 = 0$ and $\tilde{x}/\rho_0 > 0$, and (iv) the needed time τ_{ss} to reach the steady state when it exists. The value of the characteristic parameters for the different studied cases are presented in Table 1 of Paper A. Globally for $\alpha_0 > 0$, the results tend to show that Φ_{max} and w_{ss}/ρ_0 decrease with increasing κ . Although τ_{ss} is relatively similar for the cases with positive β , it decreases for increasing κ for $\beta < 0$ and $\kappa > 1/4$. For $0 > \kappa \operatorname{sgn}(\beta) \geq -3/16$, a steady state was never reached but, based on the phase diagram in Figure 13, the whole system is expected to turn into stable second phase with possible retained metastable solid solution. In the case where $\kappa \operatorname{sgn}(\beta) = -1/4$, the system was still slowly evolving during the calculation of the second phase expansion and it was found that a very large computing time is necessary to reach the steady state predicted by the analytical solution. The analysis of the data collected for $\alpha_0 < 0$ shows that the evolution of the system is much faster than when $T > T_{c_0}$. The picked-up characteristic times for $T < T_{c_0}$ are approximately half as large as those for $T > T_{c_0}$. Hence, as expected, the transformation is quicker for a quenched system. Even though the whole

material is expected to transform into second phase in defect-free conditions when $T < T_{c_0}$, the crack-induced stress enhances the transformation and accelerates it.

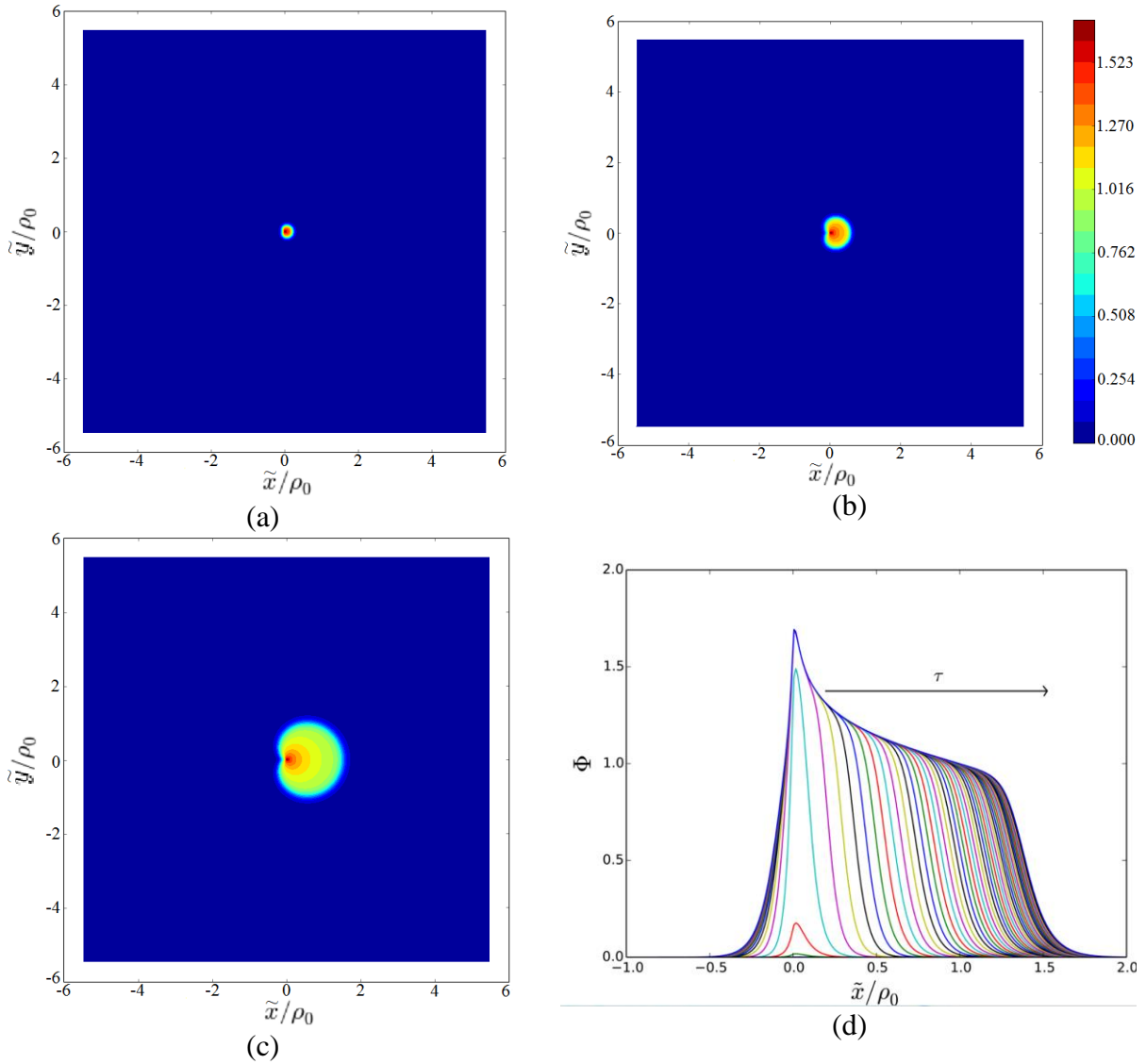


Figure 14: Evolution of the order parameter in a 2d space, which contains a crack, for (a) $\tau = 5$, (b) $\tau = 10$, (c) $\tau = 100$ and (d) in one dimension for $\tilde{y}/\rho_0 = 0$. The evolution is indicated by an arrow.

6.1.3 Further remarks

A comparison of the analytical steady-state and the numerical solutions is depicted in Figure 15. It is shown that, except at the interface between phases, the analytical and numerical steady-state solutions are similar. The local analytical solution for steady state presented in section 6.1.1 is therefore a good approximation for this model. However, the interface thickness and the kinetics of the microstructural changes can only be represented numerically by including the Laplacian and temporal terms in Eq. (36).

In addition, in Paper A, it is demonstrated that the material properties affect the results as well as the load. For instance, when K_I increases so does ρ_0 . Consequently, the presence of a crack induces phase transformation on a larger area as it propagates or the external load increases.

At this stage, the metastable phases predicted by the analytical formulation are not revealed in the numerical results. When calibrated, this model could allow estimating the kinetics of hydride precipitation in crack-tip vicinity and contribute to the prediction of hydride-related failure risk. This can be done with numerical efficiency as only one equation is solved numerically.

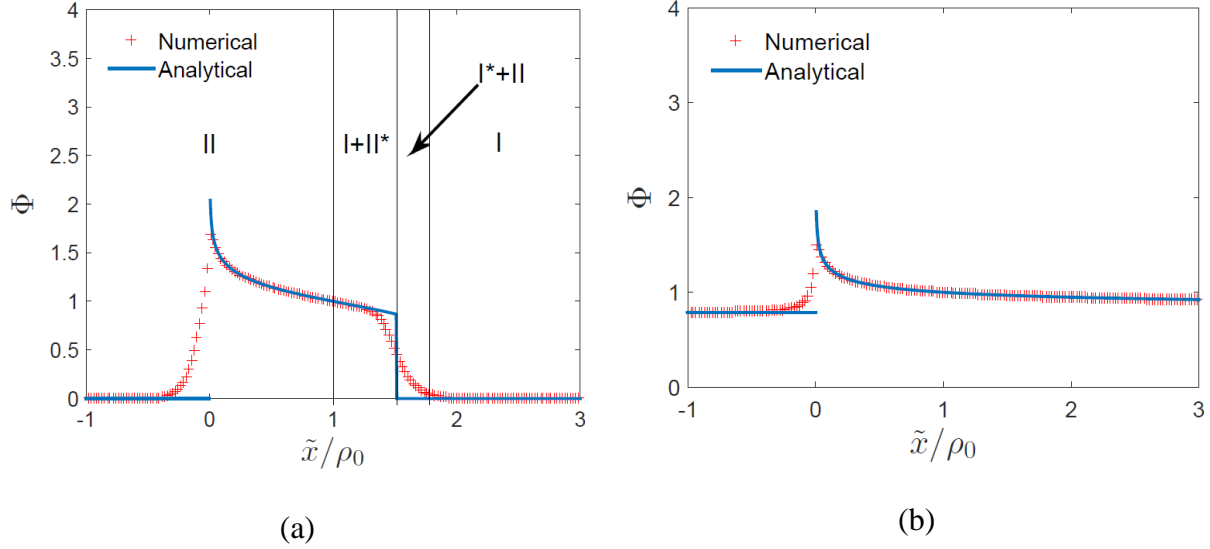


Figure 15: Comparison between steady-state solutions obtained analytically and numerically for (a) $T > T_{c_0}$ and $\kappa \text{sgn}(\beta) = -1$, and (b) $T < T_{c_0}$ and $\kappa \text{sgn}(\beta) = 1$.

6.2 Paper B

In the second paper, model 1 is applied to two anisotropic HCP metals, which can form hydrides: Zr and Ti. The considered systems are single crystals, which are initially cracked, at a temperature T and for a given constant concentration of hydrogen. The precipitation kinetics of the second phase is investigated in basal and prismatic planes. In addition, the effect of the crystallographic crack orientation on second-phase formation is examined. The used material data is summarized in Table 1 of Paper B. Equation (36) is solved for $\alpha_0 > 0$, i.e. $T > T_{c_0}$, $\beta < 0$, and $\kappa = 1$.

The different morphologies for Ti are illustrated for different planes and crack orientations ζ in Figure 16. The general observation is that a second-phase precipitate form in a confined region around the crack tip. Regardless of the considered material, the second-phase formation follows the pattern described in section 6.1.2 and is depicted in Figure 16 for Ti. The behavior of both materials is isotropic in the basal plane. Thus, the steady-state appearances of the second phase in Zr and Ti are the similar in the basal plane regardless of the crack orientation. In the prismatic planes, the change of crack orientation can induce asymmetric and/or elongated morphologies in the \tilde{y} direction. A more detailed description is given in the paper. In the basal planes, the second-phase shape obtained with Zr appears to be larger than that in Ti. In the prismatic plates, the opposite result is observed. Thus, the model

is able to capture the fact that the geometric configuration of the crack and the constitutive properties of the material affect size and shape of a forming hydride.

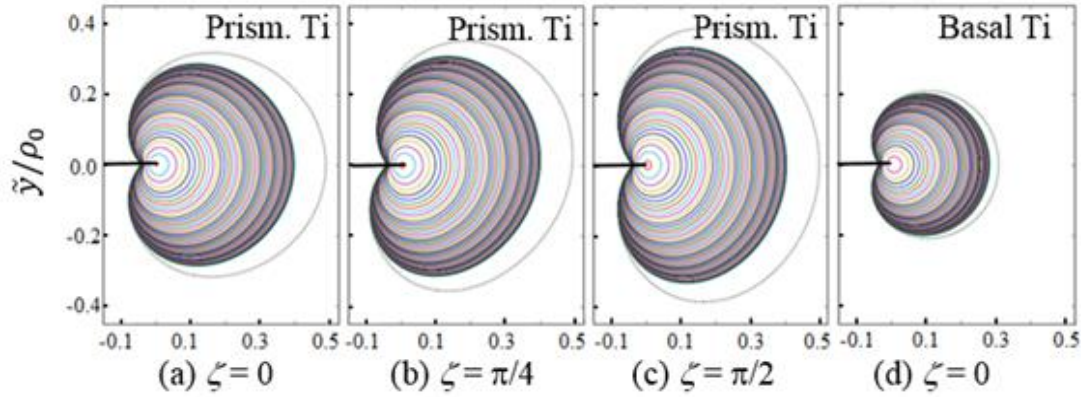


Figure 16: Evolution of $\Phi(\tilde{x}, \tilde{y})$ in a-c) the prismatic planes of Ti for $\zeta = 0, \pi/4$ and $\pi/2$, and d) the basal plane. Each line represents $0.1 \Phi_{mp}$ for each case for τ in $[0, 50]$ every twenty $\Delta\tau$.

The characteristic parameters of the transformation kinetics are summarized in Table 2 of Paper B. The investigation of the collected data allows showing the following results. First, the system reaches a steady state earlier in the basal plane than in the prismatic plane, which may come from the fact that the precipitate is smaller in the basal plane at steady state. Moreover, the time required to reach an overall steady state is found independent of the crack inclination in the respective crystallographic planes. Finally, the steady-state vertical length of the second phase as presented in Figure 16 is reached earlier than its steady-state horizontal counterpart.

In order to represent hydride formation more realistically, in particular on larger time scale, for which hydrogen atoms are observed to migrate following the stress gradients, it is necessary to include the diffusional character of the phase transformation. To this end, a composition phase-field variable can be added to the problem and coupled to the structural order parameter. The latter can also be formulated as a multi-component field in order to possibly represent the different orientations and crystal structures of the forming hydrides [82]. The work done in this paper mainly shows the possibility to incorporate LEFM into model 1 in order to account for anisotropic elasticity within the study of second-phase formation kinetics in anisotropic materials.

6.3 Paper C

Model 2 is presented and described in Paper C, where it is also employed to account for crack-induced hydride precipitation at a grain boundary in a Ti64 microstructure. The considered system is composed of two grains of α phase with different orientations and separated from each other by a smooth interface as described in section 5.5.1. In this study, precipitation is chosen to be driven by a near crack-tip stress field for cases with intragranular and intergranular cracks opening in mode I. The intragranular cracks are set perpendicular to the grain boundary. In this situation, the crack-tip/grain boundary distance is varied. In

addition, the impact of grain boundary energy on second-phase formation kinetics is examined by varying the value of s for both types of cracks.

As depicted in Figure 17a-c, hydride precipitation is found to occur in two different confined regions for an intragranular crack: (i) immediately ahead of the crack tip and, (ii) in the interface between the two crystals of the same phase. For an interface crack, a second-phase region is observed to form from the crack tip with a rapid expansion along the grain boundary. Two hydride sub-regions can be distinguished in the precipitate as illustrated in Figure 17f: one immediately ahead of the crack-tip and one further in the grain boundary. In both crack configurations and at the beginning of the simulations, a phase separation is noticed after a few steps as presented in Figure 17a-b. Examples of microstructures with an intragranular and an intergranular crack at the end of the simulations are illustrated in Figure 17c and Figure 17f respectively. In terms of precipitation kinetics, two distinct stages arise from the results: a quick nucleation followed by a slower growth. For large distances, d , between intragranular crack-tip and grain boundary, second-phase formation is observed to only occur in the near crack-tip region. At a given time of simulation, the hydride region formed in the grain boundary results larger with a decrease of d . In contrast, hydride formation kinetics in the near crack-tip area is found to be independent of d . For small d , the near-crack tip and the grain boundary hydride regions are observed to coalesce within the time of simulation, as depicted in Figure 17e.

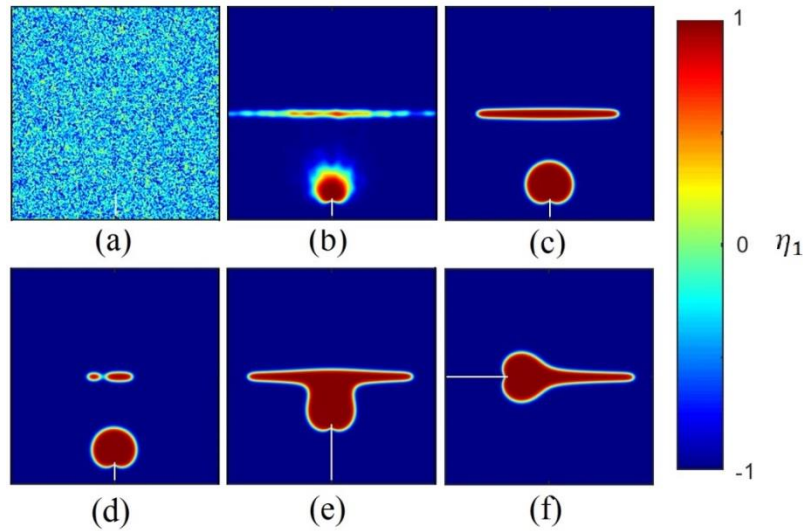


Figure 17: (a)-(c) Evolution of crack-induced hydride formation near a grain boundary; (d) Coalescence of hydride phase regions along the grain boundary; (e) Coalescence between the near-crack hydride region and that in the grain boundary; (f) Interface crack-induced hydride formation. Figures (c)-(f) display the microstructure at the end of the simulations.

The change in nucleation energy barrier has a similar effect as the variation of d . No coalescence has been observed between the two second-phase regions when s is varied, i.e. the hydride region along the grain boundary remains confined in the interface thickness while the near crack-tip hydride region remains unchanged as expected. By decreasing d or the nucleation energy barrier in the interface between the matrix phases, shorter nucleation starting time are observed in the grain boundary. For specific d and s , several distinct hydride

regions are predicted to possibly appear in the grain boundary before they coalesce as they grow, see Figure 17d.

In case of an interface crack, the decrease of the nucleation energy barrier in the grain boundary results in the elongation of the hydride region along the α/α interface. In particular, it is noticed that the total volume fraction of precipitate increases more quickly for an intergranular crack configuration than for a considered intragranular crack one in the first stage of phase transformation for a given nucleation energy barrier. However, this quantity results larger for intragranular cracks lying at small distances from the α/α interface than for intergranular cracks.

By simply representing the stress field with its analytical expression and the energy of a grain boundary by varying a single parameter, this methodology can contribute to the prediction of stress-induced phase transformation kinetics in polycrystalline microstructures, with a relatively low computational cost.

6.4 Paper D

As displayed in Table 1, model 2 as employed in paper C does not account for anisotropic transformation-strains, which are related to the phase transformation-induced dilatation of the system and the orientation of the precipitate. In addition, model 2 is limited to a single matrix phase, while many materials possess multi-phase microstructures. As mentioned in section 5.2, these aspects can be treated with model 3. The latter is presented and described in paper D. The objective of the paper is to demonstrate the potential of the methodology by modeling precipitation in proximity of stress concentrators. The main aspects that are taken into account in the approach are the effects of external stresses, the phase transformation-induced expansion of the system, the solid solubility limit in stress-free conditions, the interfacial energy related to the transition between the matrix and the precipitate phases, and the reduced nucleation energy barrier within the grain/phase boundaries on the multi-phase microstructure evolution with a numerically efficient approach. To demonstrate the capabilities of the model on a concrete example, model 3 is applied to interface crack-induced hydride precipitation at grain and phase boundaries in a typical Ti64 microstructure that contain α - and β -phase regions, see Figure 2. The hydride phase assumed to precipitate is δ -hydride even though it may be different according to experimental observations [54]. Different sets of parameters are investigated such as the energy of the phase/grain boundary and the applied stress are varied to study their effect on the kinetics of the microstructural changes.

6.4.1 Analysis of the model

The TDGL equation, i.e. here Eq. (48), is analytically examined in order to predict the stability and metastability of the different considered phases, depending on the applied stress, the phase-transformation strains, the stress-free solid solubility limit of solute, and the energy of the grain/phase interface. To this end, the equation is simplified by neglecting the Laplacian term. By doing so, singularities, discontinuities and sharp transitions/interfaces arise. The time-derivative term is then set to zero in order to identify the roots of the sum

$\partial\psi_{bulk}/\partial\eta_1 + \partial\psi_{el}/\partial\eta_1$. For these values of η_1 , the total free energy density of the system possesses minima, which corresponds to the stability or metastability of the different phases.

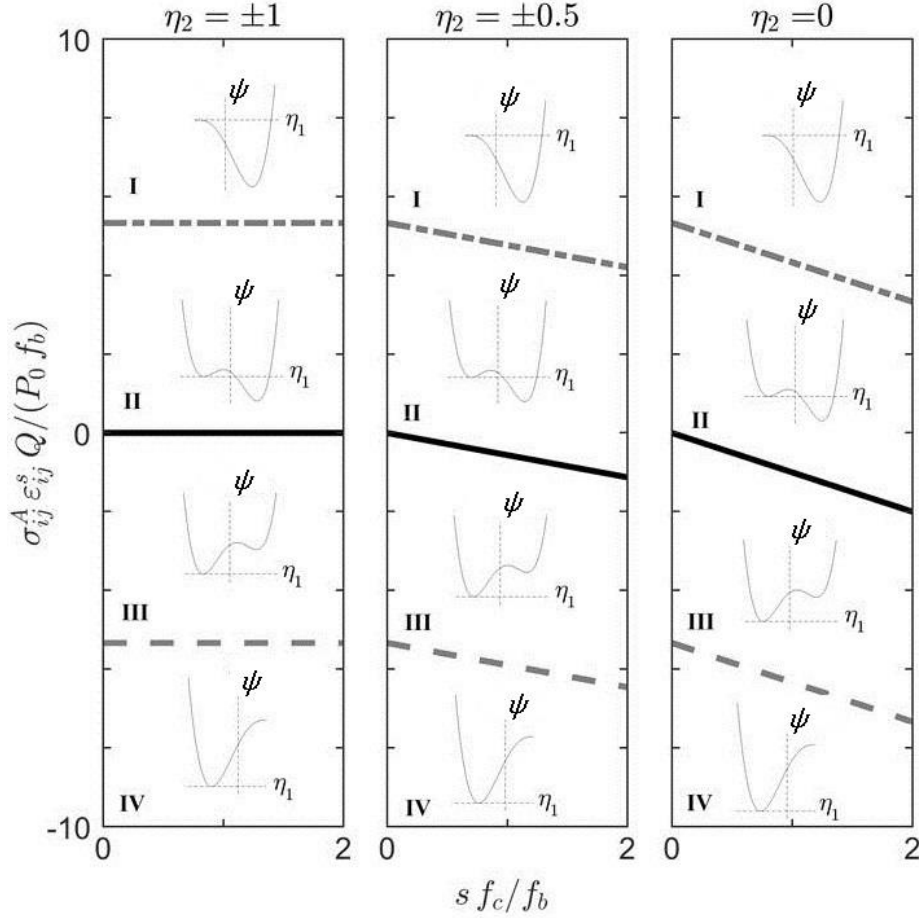


Figure 18: Phase diagrams obtained at equilibrium and by omitting the gradient free energy term. Along the stability line, the continuous one, all phases are stable. The dashed lines represent transition lines, beyond which a metastable phase becomes unstable. The appearance of the bulk free energy density is drawn in each region of the phase diagram.

This analysis results in the creation of phase diagrams, which are illustrated in Figure 18. Each phase diagram is different depending on the considered area of the material, i.e. $\eta_2 = \pm 1$ indicates a position away from the α/α or α/β interfaces, and $\eta_2 = \pm 0.5$ and $\eta_2 = 0$ designates different locations within the grain or phase boundary between the matrix phases. Four distinct regions are found. The phase diagrams indicate that the precipitate phase is stable in regions I and II while metastable in region III and unstable in region IV. The solid-solution phases are expected to be stable in regions III and IV but metastable in region II and unstable in region I. In two upper regions of the phase diagrams, an increase of the sum $\sigma_{ij}^A \epsilon_{ij}^S$ or a decrease of the stress-free solid solubility limit is expected to promote phase transformation. Figure 18 also reflects that precipitation should be favored in the interface between the matrix phases, where the nucleation energy barrier is lower than in the bulk, i.e. $s > 0$. The quantities considered in the phase diagrams are understood to cause a shift in the solid solubility limit of the system, promoting or hindering phase transformation, as seen in papers A and B. It is also noted that the increase of elastic-strain energy in the grain /phase boundary makes the slope of the total free energy density of the system steeper around the

minima. This implies a quicker phase transformation in case of a global minimum for $\eta_1 = 1$. Thus, for a given concentration of solute, a positive applied stress, an energetic phase/grain boundary or their combination should enhance hydride precipitation, which is in line with the observations made in the literature [42, 54].

6.4.2 Numerical results

The material system considered for the application of model 3 consists of two-phase regions, separated by a smooth interface along which a crack is lying. For simplicity, elastic isotropy is assumed for all phases. For the simulations, the physical quantities chosen as input parameters are considered to be realistic as they are based on observations and calculations made in the literature, and reasonable assumptions as described in the paper. The constant concentration of hydrogen is set below the stress-free solid solubility limit of the α - and β -phases. The kinetics of hydride precipitation is examined for the following configurations: an opening crack lying in an α -phase crystal, along an α/α grain boundary and along an α/β interface. In the paper, both isotropic and anisotropic stress-free strain components are regarded. These configurations are modeled by using LEFM applied to interface cracks, i.e. the applied stress term is replaced by the analytical expression of a near-interface crack stress field given by Eq. (14). In the studied situations, the remote stress is applied in the plane of the crack and perpendicular to the defect direction only.

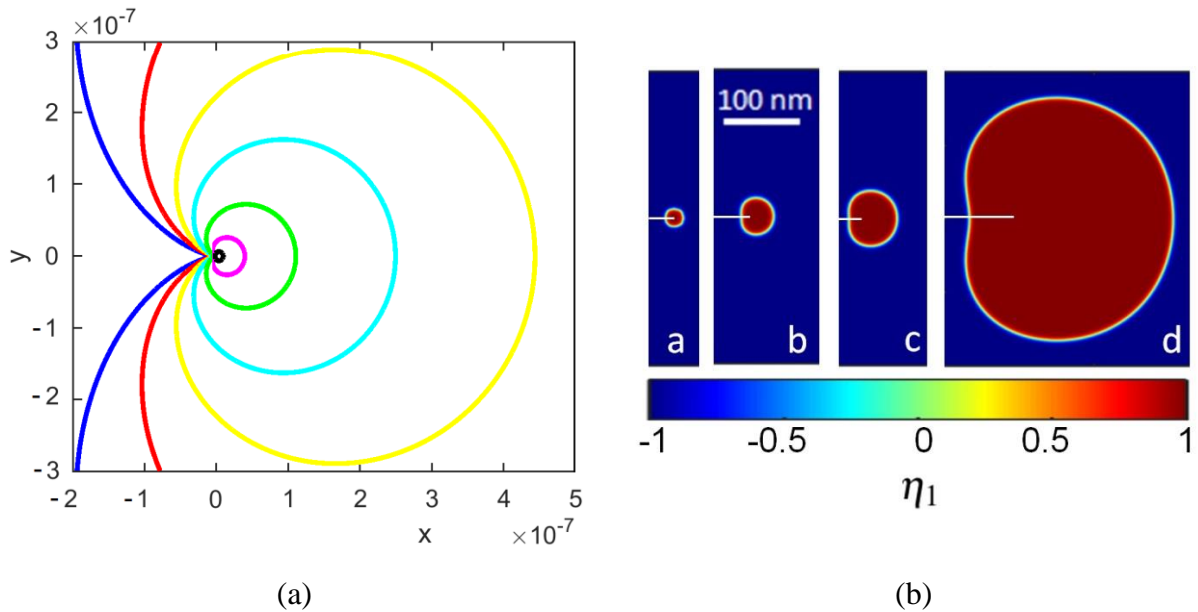
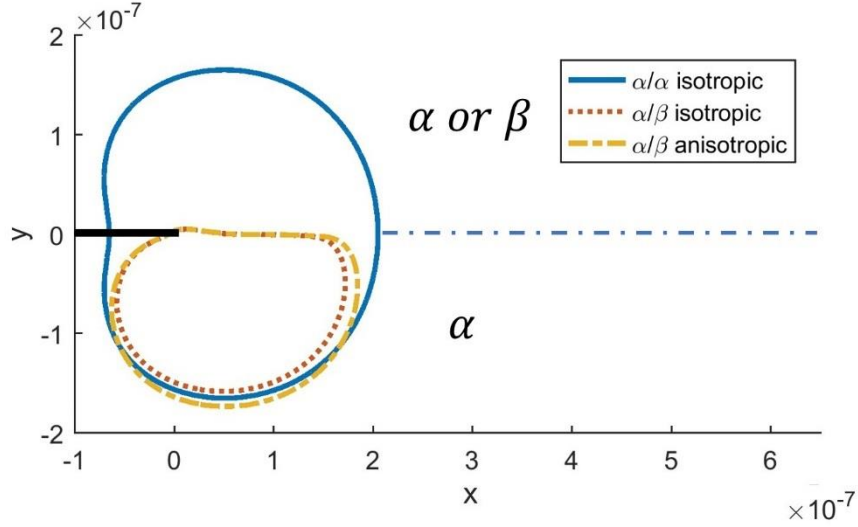


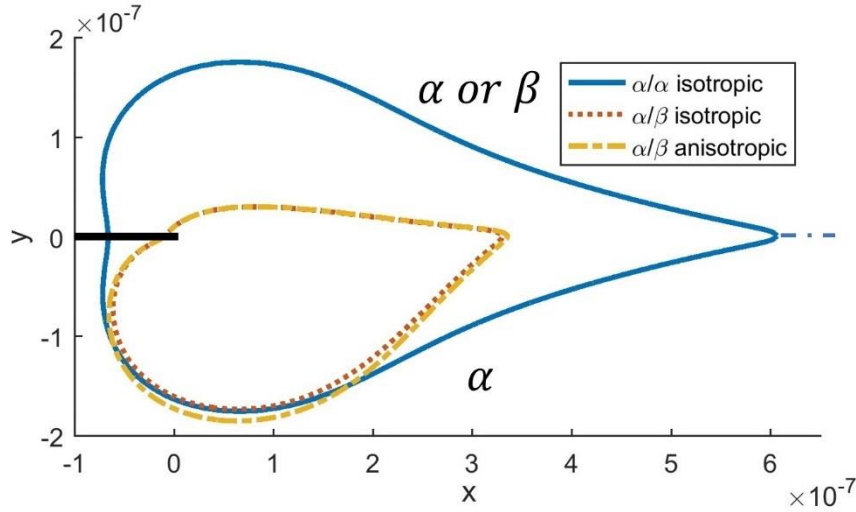
Figure 19: (a) Isostress contour for the hydrostatic stress around a crack lying within an α phase region. (b) Distribution of η_1 , i.e. appearance of the microstructure, at (a) $\tau = 0 \Delta\tau$, (b) $\tau = 500 \Delta\tau$, (c) $t = 1000 \Delta\tau$, and (d) $t = 8000 \Delta\tau = \tau_{final}$ for $s_0 = 0.0$ at an α/α interface. The solid solution appears in dark blue and the δ -phase in red. The interface crack position is indicated by a white line.

The information provided by the results indicates that the hydride formation occurs from the nucleus preliminary placed at the crack tip and mainly following the isostress lines around it as seen in Figure 19a-b. This is coherent with the fact that precipitation is driven by stress. Figure 19b illustrates the evolution of the microstructure for an opening crack lying in a crystal of phase α . The difference between the isostress lines and the contour geometries is to

be attributed to presence of the interfacial energy relative to the α/δ and β/δ transitions through the gradient free energy term, which tends to reduce the areas covered by interfaces. These differences are visible behind the crack front for all studied situations for which a precipitation takes place, and in proximity of the grain/phase boundary for $s_0 > 0.0$, see Figure 20a-b.



(a)



(b)

Figure 20: End-of-simulation position of the α/δ and the β/δ interfaces for (a) $s_0 = 0.0$ and (b) $s_0 = 2.0$, for interface cracks lying within an α -phase crystal, along an α/α grain boundary and a typical α/β interface considering isotropic (in blue and red) and anisotropic (in yellow) stress-free strains. The positions of the crack and the grain/phase boundary are indicated by a black thick line and a blue dashed line respectively.

For all cases with an actual hydride formation, it is found that the δ -phase region growth occurs quickly at the beginning and decelerates as time goes. This has also been observed in

the paper C. Since stress and hydride growth kinetics are directly related, this can be explained by the fact that the near-crack tip stress is a function that decreases as $1/\sqrt{r}$. An increase in applied load is observed to increase the δ -phase formation rate. Additionally, in phase and grain boundaries, where the nucleation energy barrier is lower, hydride formation is enhanced. This results in an elongation of the precipitate along these interfaces as observed in Figure 20b.

The difference in material parameters in either side of an α/β interface is reflected through a slower hydride growth in phase β than in phase α as presented in Figure 20a-b. By considering a typical interface between an HCP and a BCC crystal structure, the effect of the anisotropic stress-free strain has not been revealed to be significant on precipitate growth kinetics in the time of simulations as noticed in the same figures. For relatively large energy of the interface, coalescence of several δ -phase regions has been observed. This phenomenon is in line with the coalescence events experimentally observed in [42] and [54].

The results obtained for the example studied in paper D demonstrate the capability of the methodology to capture the influence of material properties on the precipitation kinetics at a microstructural level for single or multi-phase system with numerical efficiency. In addition, the flexibility of model D allows modeling the microstructural evolution of systems containing different kinds of defects, multi-phase microstructures, morphologies of grain and phase boundaries, and loading modes. It is believed that the outlined methodology can contribute to the state of the art of numerical efficient multi-scale crack propagation prediction schemes.

6.5 Paper E

In paper E, the pilot model 4 is applied through the numerical procedure described in section 5.5.2 to solve Eq. (51). The precipitation of γ -hydride in an isotropic hydrogenated Zr alloy is used as an example to show the applicability of the model. As the dilatation of the material is highly anisotropic during formation of γ -hydride out of α -phase [32], this case of study is considered a good one to assess the model.

6.5.1 Second-phase formation in a defect-free medium

First, the approach is applied to a defect-free medium. An example of the microstructure change captured by the simulations is illustrated in Figure 21. Initially, a differentiation of the phases is observed to occur as seen in Figure 21a-b. During this stage, material regions with $\varphi \rightarrow -1$ and others with $\varphi \rightarrow 1$ emerge from the initial random distribution of φ . Thereafter, the separation of phases takes place and elongated shaped hydrides ($\varphi = +1$) are found to coexist in the matrix ($\varphi = -1$), see Figure 21c. Later, the microstructural evolution tends to promote the growth of large hydrides at the expense of small precipitates, which ultimately disappear, see Figure 21c-d. An average preferential direction of hydride formation is noticed perpendicular to the applied load as described in section 2.2.2. The increase of the interfacial energy is observed to induce a decrease of the volume fraction of hydride. The applied displacement rate is found to influence the number of precipitates and the hydride growth rate.

The elastic-strain energy of the medium exhibits a plateau during phase transformation. More details about this parametric dependence of the hydride formation are given in Paper E.

The analysis of the results shows that the employed approach is able to capture the effect of interfacial energy, anisotropic eigenstrains and displacement rate on second phase formation kinetics. In addition, the influence of stress on the orientation of the formed precipitates is represented. Finally, stress relaxation is reflected in the results by absorption of the elastic-strain energy during phase transformation.

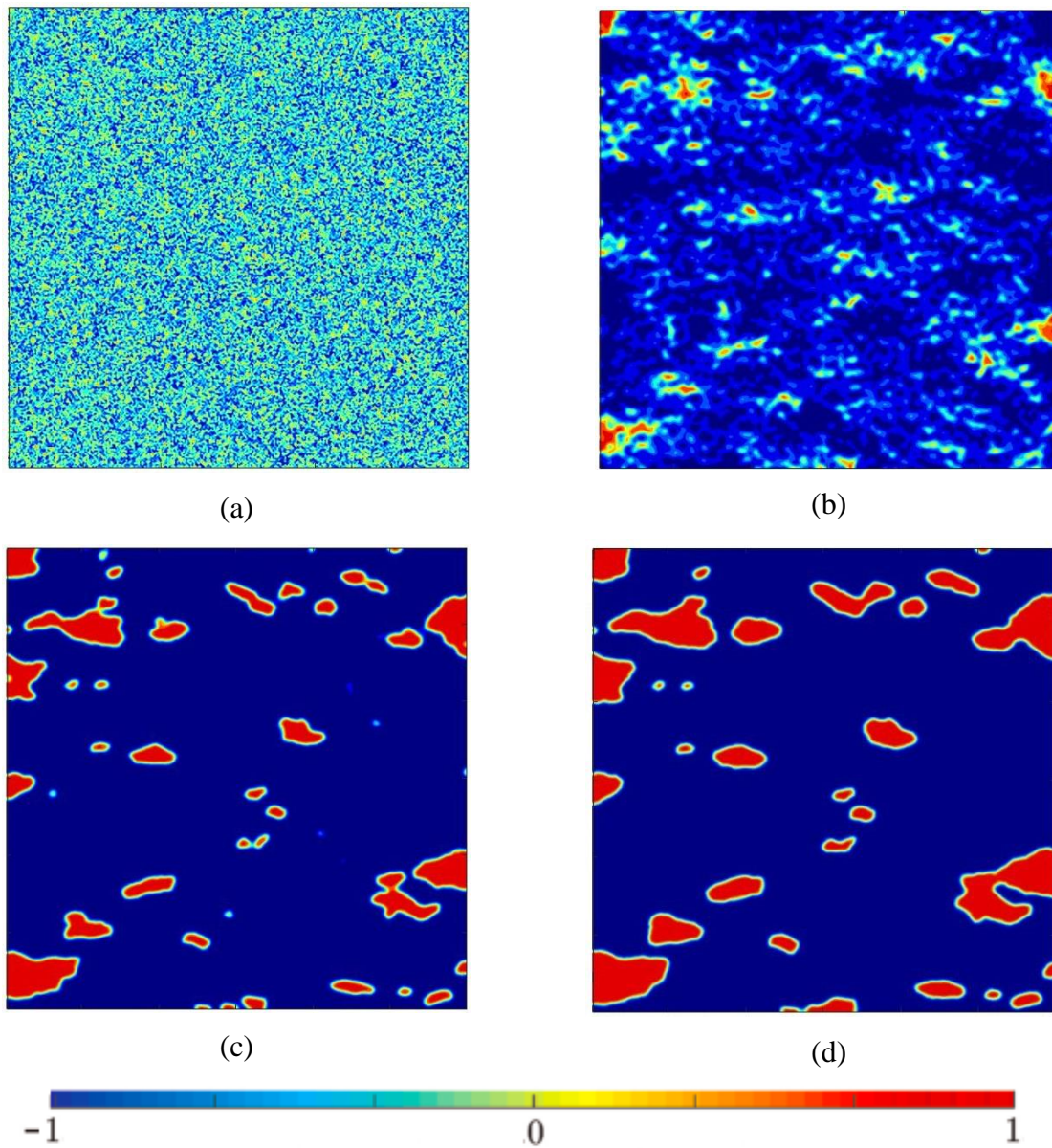


Figure 21: Distribution of the order parameter over the considered domain as time increases. Dark blue accounts for the presence of solid solution ($\varphi = -1$) and red corresponds to the presence of second phase ($\varphi = +1$). Intermediate colors indicate the position of the smooth interfaces between the phases.

6.5.2 Further works and remarks

Preliminary results for a notched body can be seen in Figure 22. Once again, the microstructural evolution starts with phase differentiation out of the initial random distribution as illustrated in Figure 22a-b. Thereafter, hydrides form around the notch tip, see Figure 22c. The number of hydrides is shown to gradually vary with the stress gradient around the notch tip. Thus, a larger density of hydride phase is found localized directly underneath the flaw tip than further around. The distribution of the hydrides is reminiscent of the non-uniform hydrostatic stress ahead of a notch tip as in the micrograph presented in [114].

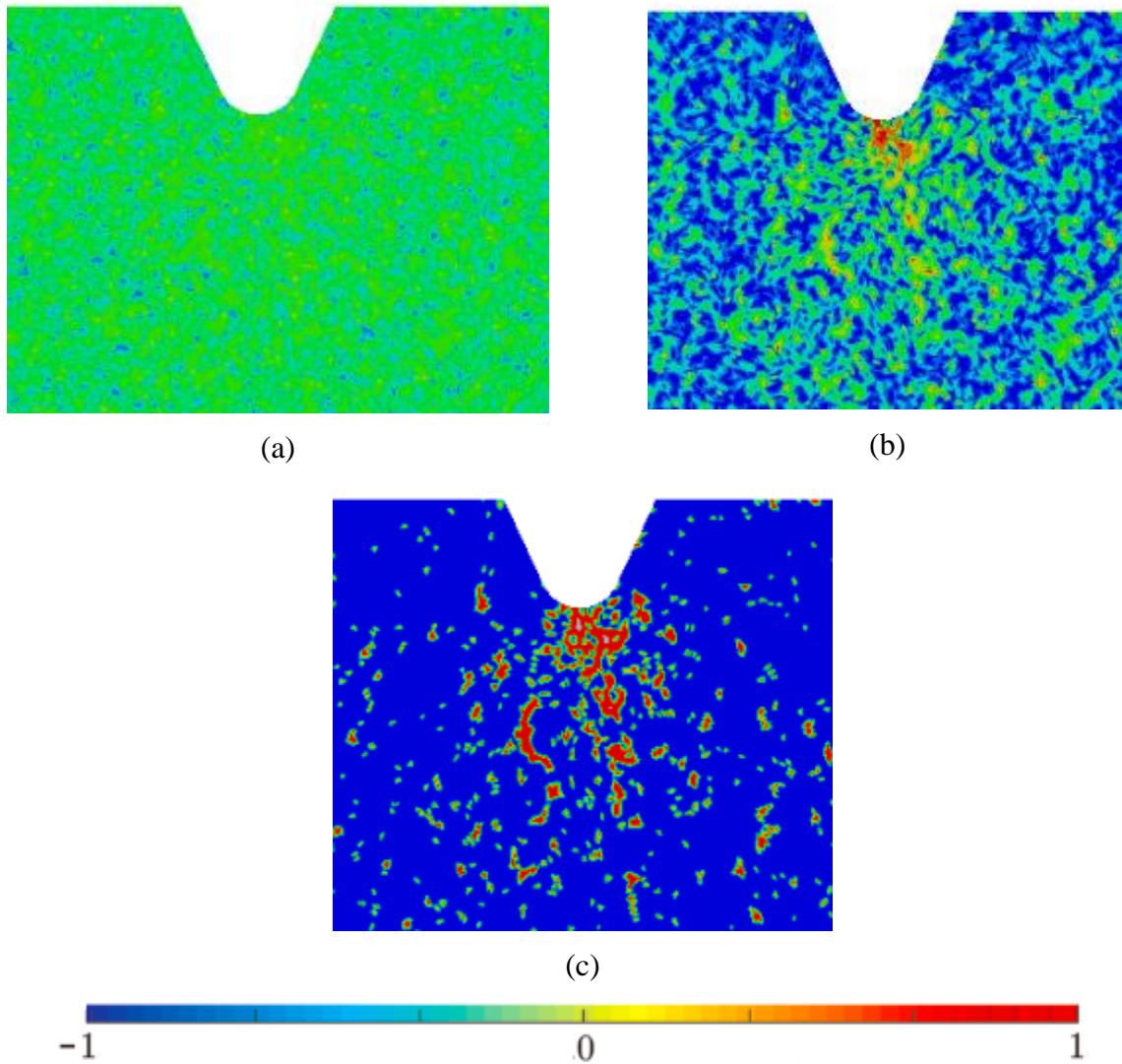


Figure 22: Distribution of the order parameter over the considered notched domain as time increases.

7 Discussion and future works

In the present section, we identify characteristics of the different models and the associated numerical methodologies as advantages or limitations. Some of them can be seen in Table 1.

7.1 Assets

Unlike the other models presented in this thesis, model 1 is capable to represent two transition orders, which is usually not done with other approaches. In particular, models 2-4 are formulated to account solely for first order transitions. Additionally, by formulation, it is possible to explicitly control the material temperature and the transition temperature with model 1.

With models 2-3 the bulk free energy is expressed such that systems composed of several grains of the same phase type with different orientations, and different phase regions can be modeled. Moreover, the energy of grain/phase boundary can be control by a single parameter and, through the parameters g_{ij} and $a_{ij} P_0$, the specific interfacial energies of the different considered transitions and realistic interface width can be accounted for. Unlike model 1, the anisotropic eigenstrains can be taken into account without having to numerically solve the equations describing mechanical equilibrium. Furthermore, the formulation of models 2-3 is such that the number of phenomenological coefficients is reduced compared to model 1. Therefore, less input data is necessary to calibrate these models.

The main advantage with models 1-3 is that mechanical equilibrium does not have to be solved numerically as the applied stress is incorporated analytically. In this manner, only the TDGL equation needs to be solved to model the microstructural changes. Thus, difficulties connected to the explicit modeling of stress field induced by singularities, such as crack tips and dislocations, can be avoided.

Model 4 has the capability to capture the orientation of the second phase region relative to anisotropic swelling due to lattice mismatch and the direction of the applied load, as observed in the literature for hydride precipitates [6].

The numerical methodology associated with the implementation of model 4 is the main advantage of the approach as more microstructural configurations than those presented in this thesis can be modeled with it. For instance, the flexibility of the boundary conditions is such that complex applied mechanical loads, which cannot be formulated analytically, can be considered. In particular, displacements with different rates can be applied to the boundary in lieu of a single stress. Moreover, the use of a fully coupled approach to solve the phase-field and mechanical equilibrium equations is an advantage over a segregated approach in terms of convergence in case of strongly-coupled problems [119].

7.2 Discussions

With models 1 and 4, only two phases can be considered, i.e. the solid-solution and the precipitate, because only a single component phase-field variable is used. However, more phases can be represented with models 2 and 3 as a two-component variable is employed.

In the framework presented for models 2 and 3, second/third-phase formation can be solved exclusively with the TDGL equation for special cases such as those for which the analytical expression for the external stress field is known. In other cases, the mechanical equations need to be solved numerically reducing the numerical efficiency of the methodology. The numerical solving of coupled equations can be achieved for all models, for example, by using the numerical methodology developed for model 4 as mentioned in the previous section.

In multi-phase or polycrystalline systems, the energy of the grain/phase boundaries varies with the misorientation angles, which indicates the level of coherency of the interfaces, cf. Chapter 3 in [126]. In [127], the energy of a grain boundary was included as a function of the misorientation angle in an additional energy term and the results displayed significant differences in terms of second-phase precipitation as the misorientation angle was varied. With models 2 and 3, the energy of the grain/phase boundary is controlled by the single parameter s , which is incorporated in the bulk free energy. In order to account for the energy of the grain/phase boundaries more realistically, it can be, therefore, beneficial to make s dependent of the misorientation angles.

With model 3, the difference in stress-free solid solubility limit from one matrix phase to another is chosen to be reflected in the interaction free energy term. This parameter could be incorporated in the bulk free energy instead such that the elastic-strain free energy remains purely mechanical.

For all models, the elastic constants are considered the same for the solid solution and the precipitate, although the difference between the phases are taken into account via their respective eigenstrains, solid solubility limit and specific interfacial energy with models 2-3. In this manner, the local deformation arising from heterogeneities are disregarded [82, 85]. The elastic inhomogeneities are mainly due to a difference in stiffness tensor for the precipitate and the matrix phases. In order to represent the precipitates individually it is necessary to consider different elastic constants for the different phases, e.g. via the Khashaturyan's (KHS) and the Voigt-Taylor (VTS) schemes [12, 13], and the equations satisfying mechanical equilibrium need to be solved numerically. Thus, parts of the numerical efficiency of the methods would be lost. Nevertheless, the results given by models 1-3 are considered to be fairly good approximations if it is assumed that the modeled second/third-phase regions correspond instead to regions of high density or cluster of second/third-phase compounds. This is supported by comparing the obtained results and the micrograph presented in [114] where a distribution of hydrides are concentrated around the notch of a Zr-2.5Nb cantilever.

In this thesis, the size of the domain, its discretization of the computational domain and time stepping are chosen such that the solutions of the TDGL equation converges and that the

motion of the interfaces is captured. However, because of limitation in terms of computational resources, the size of the domain might not always be large enough to capture the whole precipitation. In fact, since the interface thickness is taken to be approximately of the same order of magnitude as for a physical one ($\sim 10^{-9} - 10^{-8}\text{m}$) while precipitation can occur on different length scales, the computational domain needs to be of several orders of magnitude larger than the interface thickness. This is a limitation vis-à-vis the computational resources. Some solutions to this difficulty have been provided in the literature for several PFT problems. In solidification, Karma and coworkers have developed an approach, the thin interface limit, which is based on the fact that the interface width should disappear from the problem if it is negligible compared to other length scales [128]. This approach has been found to allow a drastic increase of timescale in the simulations [11]. Other solutions to reduce computational resources, applicable to grain growth, precipitate growth and coarsening, have been given in [129]. The idea is to increase the diffuse interface thickness without affecting the kinetics of the microstructural changes. These numerical methods combined with adaptive mesh refinement (AMR) techniques can allow for reasonable times of simulation when applied on larger computational domains. Additionally, the adaptive domain size technique presented in [130] has been shown to be efficient in reducing times of simulation when modeling dendritic growth. This methodology could also contribute to the reduction of the computational costs for modeling second/third-phase formation.

In the context of model calibration, the fitting of the different phenomenological coefficients and interpolation functions employed in all models requires a number of experiments, the use of computational thermodynamics and/or atomistic calculations. Phase-field modeling to a more detailed level can also provide useful data to this purpose, e.g. [90, 117].

7.3 Future works

Model 3 is the most advanced model of the thesis considering the number of features that it can account for, the fact that most parameters are physical and measurable, and the low computational cost to represent microstructural changes. In order to enhance computational efficiency, improvements are to be made on model 3.

Integrating model 3 in the numerical methodology that is employed with model 4 with Abaqus user subroutines would extend its number of applications and is also thought as an important step in the development of the approach. This would allow engineers to take into account phase transformation while performing mechanical analysis of structures operating in corrosive environments by using a single industrial program.

The variation of phase/grain boundary energy with respect to misorientation is known to be significant and, therefore, should be included in the model. Thus, the scalar parameter used to control the nucleation energy barrier in the interfaces needs to be expressed in terms of misorientation angle, cf. Chapter 5 in [126], or as an orientational order parameter [11]. This is thought as a natural next step of improvement for the model considering the representation of a realistic microstructure.

As seen in the previous section, in order to predict microstructural evolution on larger scales than those considered in this work, it is necessary to find ways to reduce the computational cost. The methods provided by Shen et al. (2004) in [129] are relevant for the presented models, especially when the interface width becomes negligible compared to the precipitate size. AMR techniques are found to be suitable numerical tools to represent larger systems as they allow reducing the number of elements away from the interfaces and refine the mesh in the transition front. For instance, this meshing methodology has been successfully employed in [104] with the software Multiphysics Object Oriented Simulation Environment (MOOSE), associated to Libmesh, whose algorithm is described in [131, 132]. AMR is therefore considered for the development of the approach.

The metals considered in this thesis can display some degrees of plasticity, which can affect phase transformation. It is therefore relevant to include plastic deformation into the models. In some phase-field models, plasticity is taken into account by employing additional order parameters [133, 134]. Plastic deformation can also be modeled, by adding the stress field of dislocations in the formulation of model 3, e.g. in the same manner as in [107].

Considering crack propagation, mechanisms such as DHC, it would be beneficial to introduce a conserved phase-field variable to account for diffusion of solute and to model crack propagation, for instance, an additional phase-field variable could be used to represent the crack as in [93]. The crack propagation criterion could also take into account the reduction of the fracture toughness averaged on the region of high density of second/third phase. However, adding phase-field parameters also signifies that more equations, including the Cahn-Hilliard one, need to be solved to account for the microstructural changes.

8 Conclusion

In this work, four different phase-field approaches with increased complexity have been developed and employed to study the stress-induced precipitation kinetics in metals with low computational costs. A special focus is given to defect-induced precipitate forming.

The models are based on an energy minimization scheme through the use of the time-dependent Ginzburg-Landau equation and are formulated such that second- or third-phase formation is driven by the coupling between the phase transformation-induced strain and the stress.

The numerical methodologies considered in this thesis are based on FVM and FEM. The software programs FiPy and Abaqus are chosen to run the simulations. The applied stress is introduced in the models either by using an analytical expression or explicitly by applying appropriate boundary conditions. For the latter procedure, the mechanical equilibrium and phase-field equations are coupled by using the thermo-mechanical fully coupled solving scheme available in Abaqus but modified through user subroutines.

During the development of the models, meaningful aspects have been studied and have been implemented progressively. The main achievements lie essentially on the modification of the bulk free energy density and the elastic-strain free energy in order to consider:

- The stress field induced by intragranular and interface cracks through the use of LEFM for single and two-phase materials with isotropic and anisotropic elastic constants;
- A microstructure containing one or two matrix phases by using a bulk free energy based on a two-component phase-field variable;
- The grain/phase boundary energy through the variation of the nucleation energy barrier with a single parameter, which is integrated in the bulk free energy functional;
- The difference in solid solubility limit between the different matrix phases in a bi-material by coupling it to the stress-free strain;
- The stress dependency of the orientation of the precipitates through the rotation of the anisotropic local stress-free strain basis into the basis of the principal stress.

The approaches have been successfully employed to model stress-induced hydride precipitation within Zr and Ti-based materials. Thus, the development of the models presented in the thesis has shown the possibility to account for many relevant and important aspects involved in second or third-phase precipitation occurring in single- or multi-phase microstructures with numerical efficiency. The presented models could contribute to the cost and time efficiency of multi-scale environment-assisted embrittlement prediction schemes within commercial software serving engineering projects.

Bibliography

- [1] S. D. Cramer and B. S. J. Covino, “55. Hydrogen Damage,” in *ASM Handbook, Volume 13A - Corrosion: Fundamentals, Testing, and Protection*, S. D. Cramer and B. S. J. Covino, Eds., ASM International, 2003, pp. 809-818.
- [2] E. Kirner, D. Thelemann and D. Wolf, “Development status of the vulcain thrust chamber,” *Acta Astronautica*, vol. 29, pp. 271-282, 1993.
- [3] L. C. Fritzemeier and W. T. Chandler, “15 - Hydrogen Embrittlement—Rocket Engine Applications,” in *Superalloys Supercomposites Superceramics*, J. K. Tien and T. Caufield, Eds., Academic Press, 1989, pp. 491-524.
- [4] L. Briottet, R. Batisse, P. Bernard, C. Duret-Thual, J.-L. Heuzé, F. Martin, F. Thebault and F. Vucko, “10 - Industrial Consequences of Hydrogen Embrittlement,” in *Mechanics - Microstructure - Corrosion Coupling*, C. Blanc and I. Aubert, Eds., Elsevier, 2019, pp. 223-244.
- [5] M. P. Puls, *The Effect of Hydrogen and Hydrides on the Integrity of Zirconium Alloy Components*, : Springer-Verlag London, 2012.
- [6] T. R. Allen, R. J. M. Konings and A. T. Motta, “5.03 - Corrosion of Zirconium Alloys,” in *Comprehensive Nuclear Materials*, R. J. M. Konings, Ed., Oxford, : Elsevier, 2012, pp. 49-68.
- [7] D. O. Northwood and U. Kosasih, “Hydrides and delayed hydrogen cracking in zirconium and its alloys,” *International Metals Reviews*, vol. 28, pp. 92-121, 1983.
- [8] C. E. Coleman, “6.03 - Cracking of Hydride-forming Metals and Alloys,” in *Comprehensive Structural Integrity*, I. Milne, R. O. Ritchie and B. Karihaloo, Eds., Oxford, : Pergamon, 2003, pp. 103-161.
- [9] H. C. Chu, S. K. Wu and R. C. Kuo, “Hydride reorientation in Zircaloy-4 cladding,” *Journal of Nuclear Materials*, vol. 373, pp. 319-327, 2008.
- [10] H. K. Birnbaum, “Mechanical properties of metal hydrides,” *Journal of the Less Common Metals*, vol. 104, pp. 31-41, 1984.
- [11] N. Provatas and K. Elder, *Phase-Field Methods in Materials Science and Engineering*, 1st ed., Weinheim, Germany: Wiley-VCH, 2010.
- [12] K. Ammar, B. Appolaire, G. Cailletaud and S. Forest, “Combining phase field approach and homogenization methods for modelling phase transformation in elastoplastic media,” *Revue européenne des éléments finis*, vol. 18, pp. 485-523, 09 2009.
- [13] A. G. Khachaturian, *Theory of Structural Transformations in Solids*, Dover Publications, 2013.
- [14] M. Smith, *ABAQUS/Standard User's Manual, Version 6.9*, Providence, RI: Dassault Systèmes Simulia Corp, 2009.
- [15] C. Nigro, *Phase Field Modeling of Flaw-induced Hydride Precipitation Kinetics in Metals*, Göteborg: Chalmers University of Technology, 2017.

- [16] W. D. Callister and D. G. Rethwisch, *Materials Science and Engineering*, Eighth edition ed., John Wiley & Sons., 2011.
- [17] L. Priester, "Chapter 7 - Precipitation at Grain Boundaries," in *Grain Boundaries: From Theory to Engineering*, Dordrecht, Springer Netherlands, 2013, pp. 217-240.
- [18] K. Christmann, "Interaction of hydrogen with solid surfaces," *Surface Science Reports*, vol. 9, pp. 1-163, 1988.
- [19] P. D. Hicks and C. J. Altstetter, "Hydrogen-enhanced cracking of superalloys," *Metallurgical Transactions A*, vol. 23, pp. 237-249, 1992.
- [20] H. K. Birnbaum and P. Sofronis, "Hydrogen-enhanced localized plasticity—a mechanism for hydrogen-related fracture," *Materials Science and Engineering: A*, vol. 176, pp. 191-202, 1994.
- [21] O. Barrera, D. Bombac, Y.-S. Chen, T.D.Daff, E.Galindo, P. Gong, D.Haley, R.Horton, I. Katzarov, J. Kermode, C.Liverani, M. Stopher and F. Sweeney, "Understanding and mitigating hydrogen embrittlement of steels: atomistic to continuum review of experimental, modelling and design progress," *Journal of Materials Science*, vol. 53, pp. 6251-6290, 2017.
- [22] C. E. Coleman and D. Hardie, "The hydrogen embrittlement of α -zirconium - A review," *Journal of the Less Common Metals*, vol. 11, pp. 168-185, 1966.
- [23] M. Neikter, *Microstructure and Hydrogen Embrittlement of Additively Manufactured Ti-6Al-4V*, Luleå university of technology, 2019.
- [24] E. Zuzek, J. P. Abriata, A. San-Martin and F. D. Manchester, "The H-Zr (hydrogen-zirconium) system," *Bulletin of Alloy Phase Diagrams*, vol. 11, pp. 385-395, 8 1990.
- [25] F. D. Manchester, *Phase Diagrams of Binary Hydrogen Alloys*, ASM, 2000.
- [26] A. T. W. Barrow, A. Korinek and M. R. Daymond, "Evaluating zirconium-zirconium hydride interfacial strains by nano-beam electron diffraction," *Journal of Nuclear Materials*, vol. 432, pp. 366-370, 2013.
- [27] S. Banerjee and P. Mukhopadhyay, "Chapter 8 - Interstitial Ordering," in *Phase Transformations: Examples from Titanium and Zirconium Alloys*, vol. 12, S. Banerjee and P. Mukhopadhyay, Eds., Pergamon, 2007, pp. 717-781.
- [28] Z. Zhao, J.-P. Morniroli, A. Legris, A. Ambard, Y. Khin, L. Legras and M. Blat-Yrieix, "Identification and characterization of a new zirconium hydride," *Journal of Microscopy*, vol. 232, pp. 410-421, 2008.
- [29] T. Maimaitiyili, J. Blomqvist, A. Steuwer, C. Bjerkén, O. Zanellato, M. S. Blackmur, J. Andrieux and F. Ribeiro, "In situ hydrogen loading on zirconium powder," *Journal of synchrotron radiation*, vol. 22, pp. 995-1000, 2015.
- [30] R. L. Beck and W. M. Mueller, "Chapter 7 - Zirconium Hydrides and Hafnium Hydrides," in *Metal Hydrides*, W. M. Mueller, J. P. Blackledge and G. G. Libowitz, Eds., Academic Press, 1968, pp. 241-335.
- [31] Q.-M. Liu, Z.-H. Zhang, S.-F. Liu and H.-Y. Yang, "The hydride precipitation mechanisms in the hydrogenated weld zone of Ti-0.3Mo-0.8Ni alloy argon-arc welded

- joints,” *Advanced Engineering Materials*, vol. 20, p. 1700679, 2018.
- [32] G. J. C. Carpenter, “The dilatational misfit of zirconium hydrides precipitated in zirconium,” *Journal of Nuclear Materials*, vol. 48, pp. 264-266, 1973.
- [33] G. Welsch, R. Boyer and E. W. Collings, “15.23 Fracture Properties,” in *Materials Properties Handbook - Titanium Alloys*, Materials Park, USA, ASM International, 1994, pp. 237-239.
- [34] A. G. Lanin, I. M. Zalivin, V. N. Turchin and E. B. Boiko, “Mechanical properties of zirconium, titanium, and yttrium hydride alloys,” *Strength of Materials*, vol. 16, pp. 869-876, 1984.
- [35] P. A. T. Olsson, M. Mrovec and M. Kroon, “First principles characterisation of brittle transgranular fracture of titanium hydrides,” *Acta Materialia*, vol. 118, pp. 362-373, 2016.
- [36] L. A. Simpson and C. D. Cann, “Fracture toughness of zirconium hydride and its influence on the crack resistance of zirconium alloys,” *Journal of Nuclear Materials*, vol. 87, pp. 303-316, 1979.
- [37] P. A. T. Olsson, K. Kese, M. Kroon and A.-M. A. Holston, “Ab initio-based fracture toughness estimates and transgranular traction-separation modelling of zirconium hydrides,” *Modelling and Simulation in Materials Science and Engineering*, vol. 23, p. 045015, 2015.
- [38] S. Takano and T. Suzuki, “An electron-optical study of β -hydride and hydrogen embrittlement of vanadium,” *Acta Metallurgica*, vol. 22, pp. 265-274, 1974.
- [39] H. K. Birnbaum, “Second phase embrittlement of solids,” *Scripta Metallurgica*, vol. 10, pp. 747-750, 1976.
- [40] M. L. Grossbeck and H. K. Birnbaum, “Low temperature hydrogen embrittlement of niobium II - Microscopic observations,” *Acta Metallurgica*, vol. 25, pp. 135-147, 1977.
- [41] C. D. Cann and E. E. Sexton, “An electron optical study of hydride precipitation and growth at crack tips in zirconium,” *Acta Metallurgica*, vol. 28, pp. 1215-1221, 1980.
- [42] D. S. Shih, I. M. Robertson and H. K. Birnbaum, “Hydrogen embrittlement of α titanium: In situ tem studies,” *Acta Metallurgica*, vol. 36, pp. 111-124, 1988.
- [43] M. Maxelon, A. Pundt, W. Pyckhout-Hintzen, J. Barker and R. Kirchheim, “Interaction of hydrogen and deuterium with dislocations in palladium as observed by small angle neutron scattering,” *Acta Materialia*, vol. 49, pp. 2625-2634, 2001.
- [44] H. Z. Xiao, S. J. Gao and X. J. Wan, “In situ TEM observation of the interaction of strain-induced hydride and crack propagation in Ti-6Al-4V,” *Scripta Metallurgica*, vol. 21, pp. 265-268, 1987.
- [45] G. Östberg, “Crack propagation in hydrided zircaloy-2,” *International Journal of Fracture Mechanics*, vol. 4, pp. 95-98, 1968.
- [46] S. Seelinger and N. Stoloff, “The effect of hydrogen on deformation and fracture processes in hafnium,” *Metallurgical Transactions, Volume 2, Issue 5*, pp.1481-1484, vol. 2, pp. 1481-1484, 1971.

- [47] S. Koike and T. Suzuki, "An electron microscopic study of hydrogen embrittlement in vanadium—II," *Acta Metallurgica*, vol. 29, pp. 553-565, 1981.
- [48] H. Matsui, N. Yoshikawa and M. Koiwa, "An in situ observation of hydrogen induced crack in niobium.," *Acta Metallurgica*, vol. 35, pp. 413-426, 1987.
- [49] C. J. Beevers, M. R. Warren and D. V. Edmonds, "Fracture of titanium-hydrogen alloys," *Journal of the Less Common Metals*, vol. 14, pp. 387-396, 1968.
- [50] D. G. Westlake, "Initiation and propagation of microcracks in crystals of zirconium-hydrogen alloys," *ASM Transactions Quarterly*, vol. Vol: 56, Mar 1963.
- [51] R. N. Singh, S. Roychowdhury, V. P. Sinha, T. K. Sinha, P. K. De and S. Banerjee, "Delayed hydride cracking in Zr-2.5Nb pressure tube material: influence of fabrication routes," *Materials Science and Engineering: A*, vol. 374, pp. 342-350, 2004.
- [52] D. B. Shan, Y. Y. Zong, T. F. Lu and Y. Lv, "Microstructural evolution and formation mechanism of FCC titanium hydride in Ti-6Al-4V-xH alloys," *Journal of Alloys and Compounds*, vol. 427, pp. 229-234, 2007.
- [53] K. V. Mani Krishna, D. Srivastava, G. K. Dey, V. Hiwarkar, I. Samajdar and S. Banerjee, "Role of grain/phase boundary nature on the formation of hydrides in Zr-2.5%Nb alloy," *Journal of Nuclear Materials*, vol. 414, pp. 270-275, 2011.
- [54] J. Kim, E. Plancher and C. C. Tasan, "Hydrogenation-induced lattice expansion and its effects on hydrogen diffusion and damage in Ti-6Al-4V," *Acta Materialia*, vol. 188, pp. 686-696, 2020.
- [55] V. Perovic and G. C. Weatherly, "The nucleation of hydrides in a Zr-2.5 wt% Nb alloy," *Journal of Nuclear Materials*, vol. 126, pp. 160-169, 1984.
- [56] R. Pederson, *The Microstructures of Ti-6Al-4V and Ti-6Al-2Sn-4Zr-6Mo and their Relationship to Processing and Properties*, Luleå university of technology, 2004.
- [57] C. Nigro, L. Sun, J. Meriaux and H. Proudhon, "Microstructural simulations of the initiation and propagation of short fretting cracks in a Ti-6Al-4V contact," *Tribology International*, vol. 74, pp. 103-109, 2014.
- [58] E. Tal-Gutelmacher and D. Eliezer, "The hydrogen embrittlement of titanium-based alloys," *The Journal of The Minerals*, vol. 57, pp. 46-49, 2005.
- [59] C. E. Inglis, "Stresses in a plate due to the presence of cracks and sharp corners," *Transactions of the Institute of Naval Architects*, vol. 55, pp. 219-241, 1913.
- [60] A. A. Griffith, "The phenomena of rupture and flow in solids," *Philosophical Transactions of the Royal Society of London*, Vols. Series A, 221, pp. 163-198, 1920.
- [61] H. Westergaard, "Bearing pressures and cracks," *Journal of applied mechanics*, vol. 6, pp. 49-53, 1939.
- [62] G. R. Irwin, "The phenomena of rupture and flow in solids," *Philosophical Transactions of the Royal Society of London*, vol. 221, pp. 163-198, 1949.
- [63] E. Orowan, "Fracture and strength of solids," *Reports on Progress in Physics*, vol. 12, pp. 185-232, 1949.

- [64] G. R. Irwin, "Onset of fast crack propagation in high strength steel and aluminum alloys," *Sagamore Research Conference Proceedings*, vol. 2, pp. 289-305, 1956.
- [65] G. R. Irwin, "Analysis of stresses and strains near the end of a crack traversing a plate," *Journal of Applied Mechanics*, vol. 24, pp. 361-364, 1957.
- [66] T. L. Anderson, *Fracture Mechanics : Fundamentals and Applications*, CRC Press, 2005.
- [67] P. C. Paris and G. C. Sih, "Stress analysis of cracks," in *Fracture toughness testing and its applications*, vol. Special Technical Publication 381, West Conshohocken, USA, ASTM International, 1965, pp. 30-83.
- [68] M. L. Williams, "The stresses around a fault or crack in dissimilar media," *Bulletin of the Seismological Society of America*, vol. 49, pp. 199-204, 04 1959.
- [69] G. P. Cherepanov, "The stress state in a heterogeneous plate with slits," *Izvestia AN SSSR, OTN Mekhan, i Mashin.*, vol. 1, pp. 131-137, 1962.
- [70] A. H. England, "A crack between dissimilar media," *Journal of Applied Mechanics*, vol. 32, pp. 400-402, 06 1965.
- [71] F. Erdogan, "Stress distribution in bonded dissimilar materials with cracks," *Journal of Applied Mechanics*, vol. 32, pp. 403-410, 06 1965.
- [72] J. R. Rice and G. C. Sih, "Plane problems of cracks in dissimilar media," *Journal of Applied Mechanics*, vol. 32, pp. 418-423, 06 1965.
- [73] M. Comninou, "The interface crack," *Journal of Applied Mechanics*, vol. 44, pp. 631-636, 1977.
- [74] J. R. Rice, "Elastic fracture concepts for interfacial cracks," *Journal of Applied Mechanics*, vol. 55, pp. 98-103, 1988.
- [75] M. Comninou and D. Schmueser, "The interface crack in a combined tension-compression and shear field," *Journal of Applied Mechanics*, vol. 46, pp. 345-348, 1979.
- [76] J. R. Rice, Z. Suo and J.-S. Wang, "Mechanics and thermodynamics of brittle interfacial failure in bimaterial systems," in *Metal-Ceramics Interface*, M. Rühle, A. G. Evans, M. F. Ashby and J. P. Hirth, Eds., Oxford, : Pergamon, 1990, pp. 269-294.
- [77] X. Deng, "General crack-tip fields for stationary and steadily growing interface cracks in anisotropic bimaterials," *Journal of Applied Mechanics*, vol. 60, pp. 183-189, 1993.
- [78] J. Dundurs, "Edge-bonded dissimilar orthogonal elastic wedges under normal and shear loading," *Journal of Applied Mechanics*, vol. 36, pp. 650-652, 1969.
- [79] J. W. Hutchinson and Z. Suo, "Mixed mode cracking in layered materials," in *Advances in Applied Mechanics*, vol. 29, J. W. Hutchinson and T. Y. Wu, Eds., Elsevier, 1991, pp. 63-191.
- [80] M. Comninou, "An overview of interface cracks," *Engineering Fracture Mechanics*, vol. 37, pp. 197-208, 1990.
- [81] M. Haataja, J. Mahon, N. Provatas and F. Léonard, "Scaling of domain size during

- spinodal decomposition: dislocation discreteness and mobility effects,” *Applied Physics Letters*, vol. 87, p. 251901, 2005.
- [82] N. Moelans, B. Blanpain and P. Wollants, “An introduction to phase-field modeling of microstructure evolution,” *Calphad*, vol. 32, pp. 268-294, 2008.
- [83] R. Kobayashi, “Modeling and numerical simulations of dendritic crystal growth,” *Physica D: Nonlinear Phenomena*, vol. 63, pp. 410-423, 1993.
- [84] R. Kobayashi, “A numerical approach to three-dimensional dendritic solidification,” *Experimental Mathematics*, vol. 3, pp. 59-81, 1994.
- [85] L.-Q. Chen, “Phase-field models for microstructure evolution,” *Annual Review of Materials Research*, vol. 32, pp. 113-140, 2002.
- [86] H. Emmerich, “Advances of and by phase-field modelling in condensed-matter physics,” *Advances in Physics*, vol. 57, pp. 1-87, 2008.
- [87] C. Shen and Y. Wang, “24. Phase-Field Microstructure Modeling,” in *ASM Handbook, Volume 22A - Fundamentals of Modeling for Metals Processing*, ASM International, 2009, pp. 297-311.
- [88] I. Steinbach, “Phase-field models in materials science,” *Modelling and Simulation in Materials Science and Engineering*, vol. 17, p. 073001, 2009.
- [89] R. C. Desai and R. Kapral, *Dynamics of Self-Organized and Self-Assembled Structures*, Cambridge, : Cambridge University Press, 2009.
- [90] J. Bair, M. A. Zaeem and D. Schwen, “Formation path of δ hydrides in zirconium by multiphase field modeling,” *Acta Materialia*, vol. 123, pp. 235-244, 2017.
- [91] K. Chang, J. Kwon and C.-K. Rhee, “Role of second-phase particle morphology on 3D grain growth: A phase-field approach,” *Computational Materials Science*, vol. 124, pp. 438-443, 2016.
- [92] J. Hektor, M. Ristinmaa, H. Hallberg, S. A. Hall and S. Iyengar, “Coupled diffusion-deformation multiphase field model for elastoplastic materials applied to the growth of Cu₆Sn₅,” *Acta Materialia*, vol. 108, pp. 98-109, 2016.
- [93] J. Kiendl, M. Ambati, L. D. Lorenzis, H. Gomez and A. Reali, “Phase-field description of brittle fracture in plates and shells,” *Computer Methods in Applied Mechanics and Engineering*, vol. 312, pp. 374-394, 2016.
- [94] D. Schneider, E. Schoof, Y. Huang, M. Selzer and B. Nestler, “Phase-field modeling of crack propagation in multiphase systems,” *Computer Methods in Applied Mechanics and Engineering*, vol. 312, pp. 186-195, 2016.
- [95] P. Shanthraj, L. Sharma, B. Svendsen, F. Roters and D. Raabe, “A phase field model for damage in elasto-viscoplastic materials,” *Computer Methods in Applied Mechanics and Engineering*, vol. 312, pp. 167-185, 2016.
- [96] J. A. Stewart and D. E. Spearot, “Phase-field models for simulating physical vapor deposition and grain evolution of isotropic single-phase polycrystalline thin films,” *Computational Materials Science*, vol. 123, pp. 111-120, 2016.

- [97] M. H. M. Sulman, "Optimal mass transport-based adaptive mesh method for phase-field models of two-phase fluid flows," *Computers & Mathematics with Applications*, vol. 72, pp. 2181-2193, 2016.
- [98] D. Tourret, Y. Song, A. J. Clarke and A. Karma, "Grain growth competition during thin-sample directional solidification of dendritic microstructures: A phase-field study," *Acta Materialia*, vol. 122, pp. 220-235, 2017.
- [99] T. Wu and L. D. Lorenzis, "A phase-field approach to fracture coupled with diffusion," *Computer Methods in Applied Mechanics and Engineering*, vol. 312, pp. 196-223, 2016.
- [100] A. M. Jokisaari, "Multiphysics phase field modeling of hydrogen diffusion in δ -hydride precipitation in α -zirconium," University of Michigan, Ann Arbor, MI, USA, 2016.
- [101] L. D. Landau and E. M. Lifshitz, *Statistical Physics*, 3rd ed., vol. 1, Oxford, : Butterworth-Heinemann, 1980.
- [102] P. Ståhle and E. Hansen, "Phase field modelling of stress corrosion," *Engineering Failure Analysis*, vol. 47, pp. 241-251, 2015.
- [103] Y. Wang, D. Banerjee, C. C. Su and A. G. Khachaturyan, "Field kinetic model and computer simulation of precipitation of L1 2 ordered intermetallics from fcc solid solution," *Acta materialia*, vol. 46, pp. 2983-3001, 1998.
- [104] J. Bair, M. A. Zaeem and M. Tonks, "A phase-field model to study the effects of temperature change on shape evolution of γ -hydrides in zirconium," *Journal of Physics D: Applied Physics*, vol. 49, p. 405302, 2016.
- [105] A. R. Massih, "Phase Transformation near dislocations and cracks," *Solid State Phenomena*, Vols. 172-174, pp. 384-389, 2011.
- [106] A. R. Massih, "Second-phase nucleation on an edge dislocation," *Philosophical Magazine*, vol. 91, pp. 3961-3980, 2011.
- [107] C. Bjerkén and A. R. Massih, "Phase ordering kinetics of second-phase formation near an edge dislocation," *Philosophical Magazine*, vol. 94, pp. 569-593, 2014.
- [108] R. A. Cowley, "Structural phase transitions I. Landau theory," *Advances in Physics*, vol. 29, pp. 1-110, 1980.
- [109] J. W. Cahn, "On spinodal decomposition," *Acta Metallurgica*, vol. 9, pp. 795-801, 1961.
- [110] S. M. Allen and J. W. Cahn, "A microscopic theory for antiphase boundary motion and its application to antiphase domain coarsening," *Acta Metallurgica*, vol. 27, pp. 1085-1095, 1979.
- [111] M. E. Gurtin, "Generalized Ginzburg-Landau and Cahn-Hilliard equations based on a microforce balance," *Physica D: Nonlinear Phenomena*, vol. 92, pp. 178-192, 1996.
- [112] A. G. Varias and A. R. Massih, "Hydride-induced embrittlement and fracture in metals effect of stress and temperature distribution," *Journal of the Mechanics and Physics of Solids*, vol. 50, pp. 1469-1510, 2002.

- [113] L. O. Jernkvist and A. R. Massih, "Multi-field modelling of hydride forming metals. Part I: Model formulation and validation," *Computational Materials Science* , vol. 85, pp. 363-382, 2014.
- [114] X. Q. Ma, S. Q. Shi, C. H. Woo and L. Q. Chen, "The phase field model for hydrogen diffusion and γ -hydride precipitation in zirconium under non-uniformly applied stress," *Mechanics of Materials*, vol. 38, pp. 3-10, 2006.
- [115] A. Deschamps and Y. Bréchet, "Influence of predeformation and ageing of an Al-Zn-Mg alloy II. Modeling of precipitation kinetics and yield stress," *Acta Materialia* , vol. 47, pp. 293-305, 1998.
- [116] R. Gómez-Ramírez and G. M. Pound, "Nucleation of a second solid phase along dislocations," *Metallurgical Transactions*, vol. 4, pp. 1563-1570, 1973.
- [117] L. Thuinet, A. D. Backer and A. Legris, "Phase-field modeling of precipitate evolution dynamics in elastically inhomogeneous low-symmetry systems: Application to hydride precipitation in Zr," *Acta Materialia* , vol. 60, pp. 5311-5321, 2012.
- [118] S.-Q. Shi and Z. Xiao, "A quantitative phase field model for hydride precipitation in zirconium alloys: Part I. Development of quantitative free energy functional," *Journal of Nuclear Materials* , vol. 459, pp. 323-329, 2015.
- [119] M. Heil, A. Hazel and J. Boyle, "Solvers for large-displacement fluid–structure interaction problems: segregated versus monolithic approaches," *Computational Mechanics*, vol. 43, pp. 91-101, 2008.
- [120] A. A. Bulbich, "Nucleation on the crack tip and transformation toughness in crystals undergoing structural phase transitions," *Journal of Materials Science*, vol. 27, pp. 1070-1080, 1992.
- [121] F. Léonard and R. C. Desai, "Spinodal decomposition and dislocation lines in thin films and bulk materials," *Physical Review B*, vol. 58, no. 13, pp. 8277-8288, 1998.
- [122] L. D. Landau and E. M. Lifshitz, *Theory of Elasticity*, 2nd ed., Oxford, : Pergamon, 1970.
- [123] S. G. Kim, W. T. Kim and T. Suzuki, "Phase-field model for binary alloys," *Physical Review E*, vol. 60, no. 6, pp. 7186-7197, Dec 1999.
- [124] D. Y. Li and L. Q. Chen, "Shape evolution and splitting of coherent particles under applied stresses," *Acta Materialia*, vol. 47, pp. 247-257, 1998.
- [125] J. E. Guyer, D. Wheeler and J. A. Warren, "FiPy: Partial differential equations with Python," *Computing in Science & Engineering*, vol. 11, no. 3, pp. 6-15, 2009.
- [126] D. A. Porter, K. E. Easterling and M. Y. Sherif, *Phase Transformations in Metals and Alloys*, CRC, 2009, pp. 269-276.
- [127] X. Q. Ma, S. Q. Shi, C. H. Woo and L. Q. Chen, "Phase-field simulation of hydride precipitation in bi-crystalline zirconium," *Scripta Materialia* , vol. 47, pp. 237-241, 2002.
- [128] A. Karma and W.-J. Rappel, "Phase-field method for computationally efficient modeling of solidification with arbitrary interface kinetics," *Physical Review E*, vol. 53,

- no. 4, pp. R3017--R3020, Apr 1996.
- [129] C. Shen, Q. Chen, Y. H. Wen, J. P. Simmons and Y. Wang, "Increasing length scale of quantitative phase field modeling of growth-dominant or coarsening-dominant process," *Scripta Materialia*, vol. 50, pp. 1023-1028, 2004.
 - [130] A. F. Ferreira, I. L. Ferreira, J. P. d. Cunha and I. M. Salvino, "Simulation of the microstructural evolution of pure material and alloys in an undercooled melts via phase-field method and adaptive computational domain," *Materials Research*, vol. 18, no. 3, pp. 644-653, 2015.
 - [131] B. Kirk, J. Peterson, R. Stogner and G. Carey, "libMesh: a C++ library for parallel adaptive mesh refinement/coarsening simulations," *Engineering with Computers*, vol. 22, pp. 237-254, 12 2006.
 - [132] R. H. Stogner, G. F. Carey and B. T. Murray, "Approximation of Cahn–Hilliard diffuse interface models using parallel adaptive mesh refinement and coarsening with C1 elements," *International Journal for Numerical Methods in Engineering*, vol. 76, pp. 636-661, 2008.
 - [133] X. H. Guo, S.-Q. Shi and X. Q. Ma, "Elastoplastic phase field model for microstructure evolution," *Applied Physics Letters*, vol. 87, p. 221910, 2005.
 - [134] S. Y. Hu, M. I. Baskes and M. Stan, "Phase-field modeling of microvoid evolution under elastic-plastic deformation," *Applied Physics Letters*, vol. 90, p. 081921, 2007.

